Contrib Mineral Petrol (2016) 171:69
DOI 10.1007/s00410-016-1279-z

ORIGINAL PAPER

Elucidating the magmatic history of the Austurhorn silicic intrusive complex (southeast Iceland) using zircon elemental and isotopic geochemistry and geochronology

A. J. Padilla[1] · C. F. Miller[1] · T. L. Carley[1,2] · R. C. Economos[3,4] · A. K. Schmitt[3,5] · M. A. Coble[6] · J. L. Wooden[6] · C. M. Fisher[7] · J. D. Vervoort[7] · J. M. Hanchar[8]

Received: 28 December 2015 / Accepted: 8 July 2016 / Published online: 4 August 2016

Abstract The Austurhorn intrusive complex (AIC) in southeast Iceland comprises large bodies of granophyre and gabbro, and a mafic–silicic composite zone (MSCZ) that exemplifies magmatic interactions common in Icelandic silicic systems. Despite being one of Iceland's best-studied intrusions, few studies have included detailed analyses of zircon, a mineral widely recognized as a valuable tracer of the history and evolution of its parental magma(s). In this study, we employ high spatial resolution zircon elemental and isotopic geochemistry and U–Pb geochronology as tools for elucidating the complex construction and magmatic evolution of Austurhorn's MSCZ. The trace element compositions of AIC zircon crystals form a broad but coherent array that partly overlaps with the geochemical signature for zircons from Icelandic silicic volcanic rocks. Typical of Icelandic zircons, Hf concentrations are relatively low (<10,000 ppm) and Ti concentrations range from 5 to 40 ppm (Ti-in-zircon model temperatures = 761–981 °C). Zircon $\delta^{18}O$ values vary from +2.2 to +4.8 ‰, consistent with magmatic zircons from other Icelandic silicic rocks, and preserve evidence for recycling of hydrothermally altered crust as a significant contribution to the generation of silicic magmas within the AIC. Zircon ε_{Hf} values generally range from +11 to +15. This range overlaps with that of Icelandic basalts from off-rift settings as well as the least depleted rift basalts, suggesting that the AIC developed within a transitional rift environment. In situ zircon U–Pb ages yield a weighted mean of 6.52 ± 0.03 Ma for the entire complex, but span a range of ~320 kyr, from 6.35 ± 0.08 to 6.67 ± 0.06 Ma (2σ SE). Gabbros and the most silicic units make up the older part of this range, while granophyres and intermediate units make up the younger part of the complex, consistent with field relationships. We interpret the ~320 kyr range in zircon ages to represent the approximate timescale of magmatic construction of the MSCZ. These U–Pb data suggest that the complex was constructed by multiple short-lived magmatic intrusion events occurring closely spaced in time, allowing periodic re-melting and rejuvenation of mush-like material and a prolonged lifetime for the complex.

Communicated by Timothy L. Grove.

Electronic supplementary material The online version of this article (doi:10.1007/s00410-016-1279-z) contains supplementary material, which is available to authorized users.

✉ A. J. Padilla
a.padilla@vanderbilt.edu

[1] Earth and Environmental Sciences, Vanderbilt University, Nashville, TN, USA

[2] Geology and Environmental Geosciences, Lafayette College, Easton, PA, USA

[3] Department of Earth, Planetary, and Space Sciences, University of California–Los Angeles, Los Angeles, CA, USA

[4] Roy M. Huffington Department of Earth Sciences, Southern Methodist University, Dallas, TX, USA

[5] Institute of Earth Sciences, Heidelberg University, Heidelberg, Germany

[6] SHRIMP-RG Lab, Stanford University-USGS, Stanford, CA, USA

[7] School of the Environment, Washington State University, Pullman, WA, USA

[8] Department of Earth Sciences, Memorial University of Newfoundland, St. John's, NL, Canada

Keywords Iceland · Silicic magmatism · Austurhorn · Zircon · Geochemistry · Isotopic geochemistry · Trace elements · U–Pb geochronology · Hf isotopes · Oxygen isotopes

Introduction

Silicic rocks make up an estimated 10–13 % of Icelandic exposures (Walker 1966; Gunnarsson et al. 1998; Jónasson 2007), the largest known concentration in a modern oceanic setting. The petrogenesis of these rocks has received considerable attention, but most investigations have focused on the volcanism (e.g. Gunnarsson et al. 1998; Martin and Sigmarsson 2007; Carley et al. 2011, 2014; Bindeman et al. 2012), with less attention paid to the more sparsely exposed silicic intrusive rocks. To date, there has been no detailed study of zircons in any Icelandic intrusion. Because of its low solubility in common melt and fluid compositions, its stability and resistance to alteration at Earth's surface, and extremely slow volume diffusion within its crystal structure at magmatic temperatures (e.g. Cherniak et al. 1997a, b; Watson and Cherniak 1997; Cherniak and Watson 2000, 2007), zircon can retain valuable geochemical information about the environments in which it grew, including crystallization temperature and the composition of the melt(s) from which it crystallized, the source region, and elapsed time since crystallization (age), making it a powerful tool for investigating the evolution of silicic magmatic systems.

We have selected the relatively well-characterized Austurhorn intrusive complex (AIC) (Blake 1966; Gale et al. 1966; Mattson et al. 1986; Furman et al. 1992a, b; Thorarinsson and Tegner 2009; Weidendorfer et al. 2014) for the first detailed study of zircon from an Icelandic intrusive complex. In combination with supporting field investigation, petrography, and whole-rock elemental and isotopic geochemistry, we use zircon trace element and U–Pb, Hf, and O isotopic data to investigate the petrogenesis of the AIC. In particular, we aim to elucidate: (1) the nature of zircons in the rock types commonly associated with shallow Icelandic intrusions; (2) magmatic processes within the Austurhorn magmatic system; and (3) the origin(s) of the AIC magma(s).

Previous research has addressed generation of AIC silicic magmas using a range of petrologic and geochemical approaches. Interpretations differ, however, with some researchers advocating generation of silicic melts at Austurhorn dominantly by fractional crystallization (FC) of tholeiitic magmas (e.g. Furman et al. 1992b, Bindeman et al. 2012), whereas others favor partial melting of altered and hydrated basaltic crust as the central mechanism for generating silicic melts (e.g. Martin and Sigmarsson 2010). Furman et al. (1992b) argue that the major element composition of plagioclase and clinopyroxene from mafic units (Hvalnesfjall gabbro and MSCZ mafic pillows) support detailed field relationships between mafic and silicic units indicating fractionation of tholeiitic basalts. Bindeman et al. (2012) provide bulk mineral and in situ zircon oxygen isotopes from an AIC silicic sample that suggest a relatively homogeneous mantle-like signature (clinopyroxene δ^{18}O: +4.2 ‰; quartz: +6.03 ‰; zircon: +4.36 ‰ to +5.60 ‰). This points to derivation of magmas primarily by fractional crystallization from mantle-derived basalt. In contrast, Martin and Sigmarsson (2010) present bulk sample oxygen isotope evidence for extensive crustal recycling from intermediate to silicic samples of the AIC. They advocate partial melting of low-δ^{18}O hydrated metabasaltic crust as the dominant source, based on low whole-rock δ^{18}O values (−2.1 ‰ for a 53.6 % SiO_2 sample; +0.5 ‰ for a 64.8 % SiO_2 sample) and consistent with the presence of low-δ^{18}O clinopyroxene phenocrysts in Austurhorn samples (Furman 1989).

In this study, we build upon previous work and investigate the AIC using an approach that has not yet been applied here or to any other intrusion in Iceland: a detailed study of zircon geochronology and elemental and isotopic analyses from a representative suite of mafic to silicic samples, supported by field observations and whole-rock geochemistry and petrography. Our work supports and refines previous interpretations regarding the role of open-system processes in the AIC (e.g. Mattson et al. 1986; Furman et al. 1992a; Weidendorfer et al. 2014); more precisely dates the intrusion and constrains its duration of emplacement; suggests that both assimilation and fractional crystallization (AFC) played critical roles in generating the silicic magmas; and provides the first comprehensive data set on zircon geochemistry in an Icelandic intrusion.

Geological background

The Austurhorn intrusive complex (AIC), southeast Iceland

The AIC is a Late Miocene composite intrusion located along the coast of southeastern Iceland (Fig. 1). Cropping out over an area of 15 km^2, the AIC is one of the largest and the best exposed silicic Icelandic intrusion, equivalent in dimension to modern and Neogene Icelandic central volcanoes (Furman et al. 1992a) with similar diversity and abundance of rock types. The exposed portion of the AIC (Fig. 2) is surrounded by a ~1-km-wide contact metamorphic thermal aureole that includes roof and wall contacts in several locations, where the AIC intrudes predominantly west-dipping basaltic lavas and tuffs from the Álftafjördur and Lón Late Miocene central volcanoes (Walker 1964; Blake 1966, 1970; Ross and Mussett 1976). The intrusion

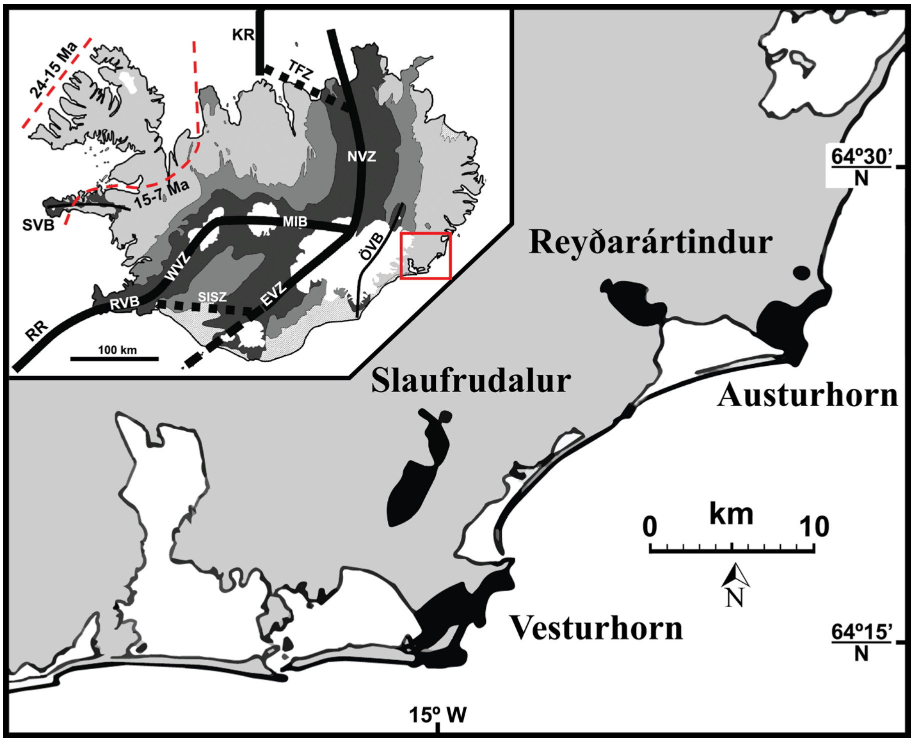

Fig. 1 Regional map of southeast Iceland outlining the four major composite silicic intrusions exposed in the area (*black shaded* areas; modified after Gale et al. 1966). *Inset*: Overview map of Iceland and its major tectonovolcanic zones (modified after Thordarson and Höskuldsson 2002, and Carley et al. 2011): Northern (NVZ), Eastern (EVZ), and Western Volcanic Zones (WVZ), Snæfellsness Volcanic Belt (SVB), Reykjanes Ridge (RR), Reykjanes Volcanic Belt (RVB), South Iceland Seismic Zone (SISZ), Öræfi Volcanic Belt (ÖVB), Tjornes Fracture Zone (TFZ), Kolbeinsey Ridge (KR), and the Mid-Iceland Belt (MIB). The *red dashed lines* represent extinct rifts (Martin et al. 2011). The *red box* indicates the location of the intrusions. The *shades* of *gray* indicate age divisions: *light gray* = Neogene (17–3.3 Ma); *medium gray* = Plio–Pleistocene (3.3–0.7 Ma); *dark gray* = upper Pleistocene to present (0.7–0 Ma); *white* = ice caps or water

comprises granophyre, gabbro, minor felsite, and an extensive mafic–silicic composite zone (MSCZ—previously referred to as the "net-veined complex," e.g. Blake 1966; Mattson et al. 1986; Furman et al. 1992a; Weidendorfer et al. 2014). Evidence for open-system behavior, including chamber replenishment by dense basaltic and buoyant silicic magmas indicated by commingling textures, is abundant throughout the MSCZ (Fig. 3; Mattson et al. 1986; Furman et al. 1992a; Weidendorfer et al. 2014). The exposed gabbro is largely restricted to the peaks Hvalnesfjall and Þúfuhraunstindur (see Fig. 2) in the central part of the complex and appears to be almost entirely encircled by granophyre (Blake 1966).

Based on the structure of the intrusion and geochemistry of the mafic and silicic rocks at AIC, previous researchers have suggested that it developed within a short-lived immature transitional rift environment, analogous to the Eyjafjallajökull and Torfajökull central volcanoes in Iceland's modern eastern neovolcanic zone (Furman et al. 1992a). The AIC is thus interpreted to represent the roots of an exhumed Neogene central volcano. Previous studies have constrained the depth of emplacement to ~2 km, primarily based on field relations and laumontite (zeolite) alteration in basaltic amygdales observed just outside the Austurhorn thermal aureole; the composition of these amygdales has been suggested to constrain the maximum depth to which basalt was buried at the time of alteration from AIC intrusions (Blake, 1966; Walker 1960, 1964). The AIC has previously been dated by K–Ar from biotite extracted from aplitic veins in the gabbroic intrusion at 6.6 ± 0.4 Ma (Moorbath et al. 1968) and by U–Pb isotope systematics in zircons from gabbro and granophyre at 6.6 ± 0.4 (2SE; $n = 15$) and 6.5 ± 0.2 (2SE; $n = 12$), respectively (Martin et al. 2011; the only previously published zircon ages for the AIC).

The mafic–silicic composite zone (MSCZ)

The Austurhorn mafic–silicic composite zone (MSCZ) occupies the lowest structural levels exposed, from the base of Þúfuhraunstindur south to the Hvalnes peninsula, and north to Krossanes point (Fig. 2) where it is bound by the surrounding homogeneous granophyre and intrudes Neogene volcanic rocks. It comprises approximately 30–40 %

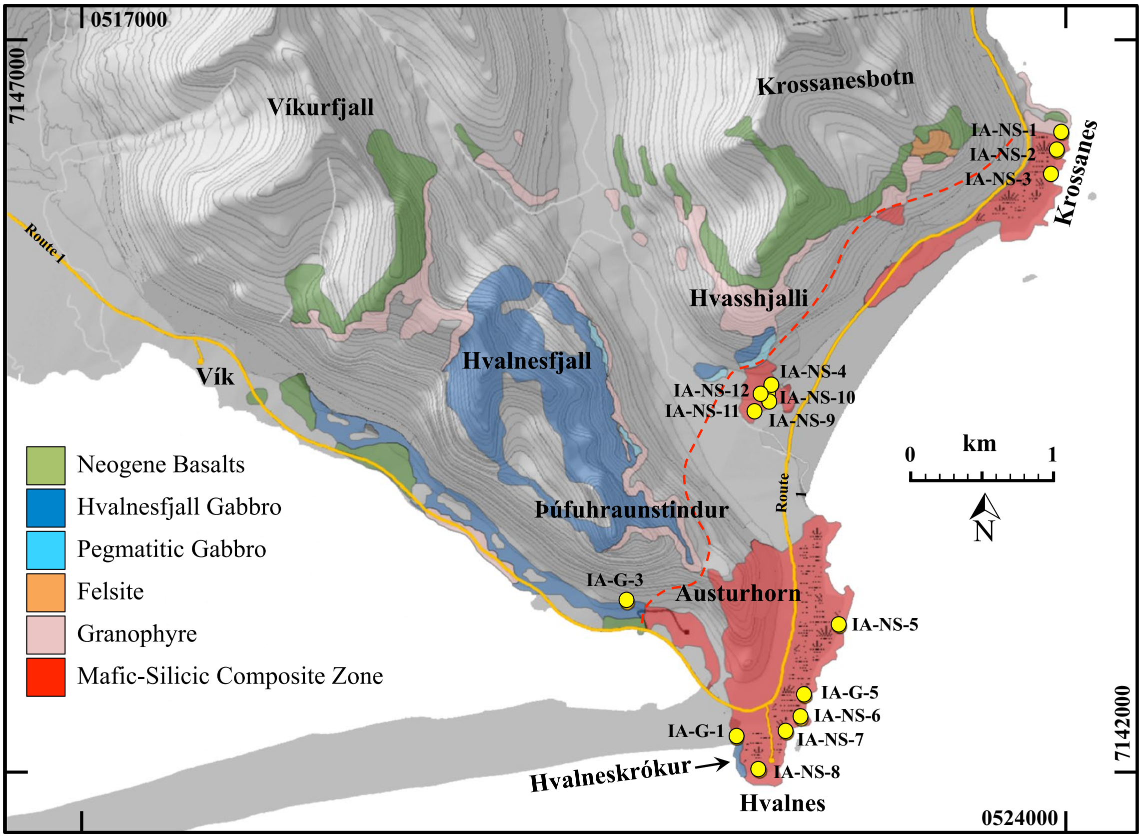

Fig. 2 Geologic map of the Austurhorn intrusive complex (modified after Furman et al. 1992b). *Yellow labeled dots* indicate sampling locations. *Gray zones* indicate unconsolidated quaternary deposits (e.g. talus and alluvium) and undifferentiated bedrock exposures. *White* areas indicate water. Iceland national Route 1 is highlighted in *yellow*. Coordinates listed are in WGS84 UTM grid zone 28W. Patterned areas within the mafic–silicic composite zone (MSCZ) denote marsh environment. The *dashed red line* indicates the implied structural top of the MSCZ

of the AIC in three main areas at the eastern margins of the intrusion (Blake 1966; Mattson et al. 1986; Furman et al. 1992a). The MSCZ contains abundant mafic to intermediate enclaves (clasts, pillows, tabular bodies) with cuspate, crenulated, or angular boundaries and entirely surrounded by silicic rock, zones of intermediate rock, and sheets of diabasic and basaltic rock (Fig. 3). The enclave density within a given outcrop is highly variable, ranging from a few volume percent up to 60 %. The margins of the MSCZ have been defined by Furman et al. (1992b) to be where a silicic host rock-bearing mafic blocks >5 cm in dimension are in contact with Hvalnesfjall gabbro or Miocene volcanics, or where mafic blocks disappear abruptly from a silicic unit without apparent change in the silicic matrix itself.

Methods

Fieldwork

Building upon field descriptions of the AIC and MSCZ by Furman et al. (1992b) and Mattson et al. (1986), we carried out field studies to further characterize the diversity of silicic rock units, the distribution and abundance of mafic bodies within the MSCZ, and the contact relationships and nature of interaction between all units (see “Field Observations” section). Eleven representative samples were collected from well-exposed outcrops of the MSCZ and surrounding gabbro and granophyre units of the AIC (see Fig. 2; Table 1 for locations and sample descriptions). In an effort to obtain the most representative zircon populations for each silicic unit, we sampled all units from the least heterogeneous exposures available. Silicic samples within the MSCZ represent the range of textures, grain size, mafic phenocryst content, and abundance of mafic material (pillows, enclaves, and/or clasts).

Whole-rock Characterization

Mineral assemblages and textural relations were characterized for all samples using thin-section optical microscopy (Table 1; see also supplementary figure S1 for samples from which we analyzed zircon). Whole-rock major and trace element abundances were determined for all samples

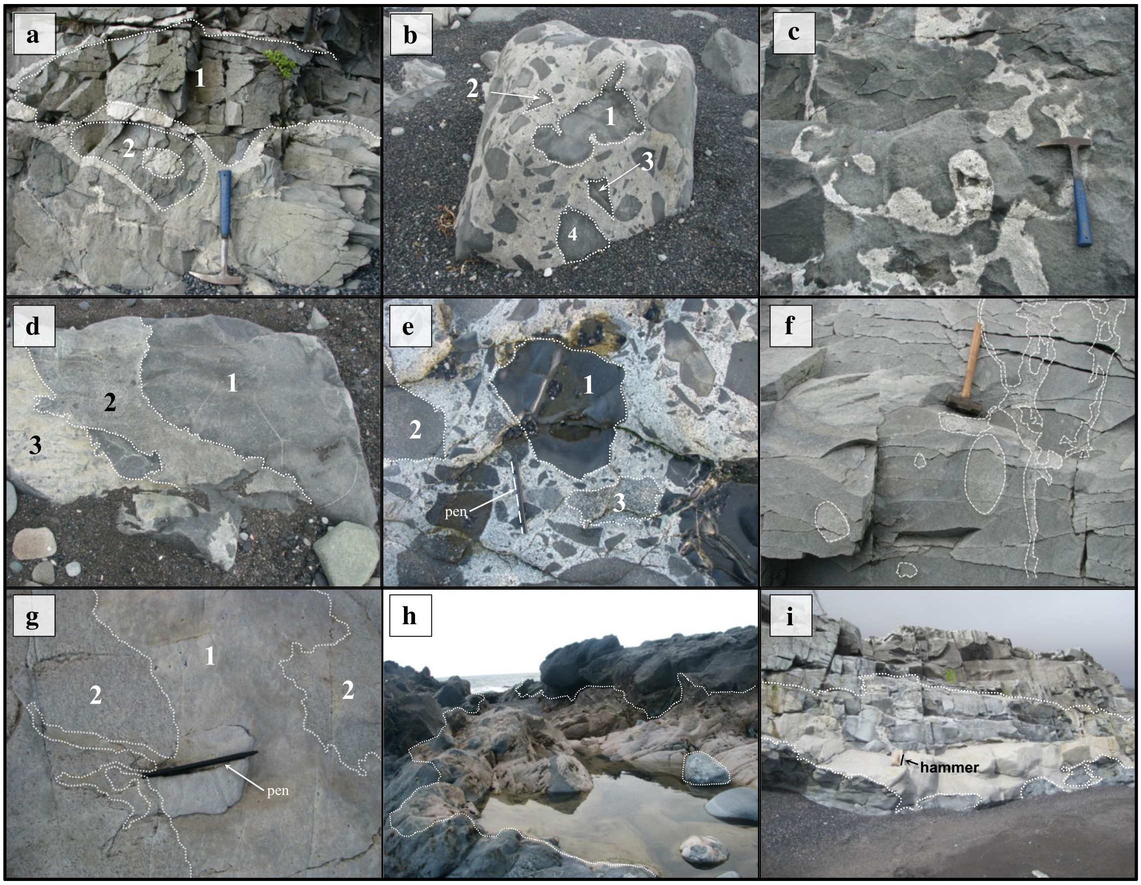

Fig. 3 Diversity of magmatic interactions found within the MSCZ: **a** mafic pillow-like structures (*1*, *2*) in intermediate host, with a notable silicic core in pillow *2*; **b** mafic pillow-like enclaves with chilled and crenulate margins (*1*, *4*), and mafic clasts with sharp and angular boundaries (*2*, *3*), in silicic host; **c** continuous and undulate dike-like silicic intrusions within a mafic host; **d** skialithic pillow ("*pillow within a pillow*"), with *dark* mafic core (*1*) surrounded by lighter hybrid zone (*2*) all within a felsic host (*3*); **e** diversity of mafic enclaves within a silicic host ranging from large clasts with angular boundaries (*1*) and less mafic enclaves with sharp boundaries (*2*), to smaller partially hybridized enclaves with diffuse boundaries (*3*) and abundant small mafic clasts (in matrix); **f** silicic pipe-like networks within intermediate host rocks; **g** felsic–felsic magmatic mingling; **h, i** mafic sheet-like intrusions with margins disaggregating into large pillows and enclaves. Scale: hammers on **a**, **c**, **f**, and **i** are ~40 cm tall; boulders on **b**, **d**, and **h** (*left center*, *dashed outline*) are ~1 m wide; pen on **e** and **g** is ~15 cm long

(for methods, see supplementary material S1; for a summary of oxide and elemental compositions see supplementary material S2).

Based on whole-rock major element compositions and Zr concentrations, we calculated model zircon saturation temperatures (ZSTs; see Table S1) for all samples using the formulation of Watson and Harrison (1983) as revised by Boehnke et al. (2013). The saturation equation requires the composition of a melt saturated in zircon, and we acknowledge that uncertainties are introduced because whole-rock compositions are not in general equivalent to melt compositions, particularly for intrusive rocks. Calculated ZSTs provide minima for the initial temperature of the magma represented by the sample, unless inherited and/or accumulated zircons are relatively abundant, which results in calculated model temperatures that exceed true magma temperatures. For most silicic intrusive rocks, calculated ZSTs are likely to be modest under- or overestimates, within tens of degrees; in contrast, ZSTs calculated from mafic whole-rock compositions are likely to severely underestimate magmatic temperatures, because mafic magmas are strongly undersaturated in zircon (e.g. Miller et al. 2003; Harrison et al. 2007; Boehnke et al. 2013; McDowell et al. 2014; Moecher et al. 2014). Given these uncertainties, we use ZSTs as estimates to generally compare model magmatic temperatures for the silicic units of the AIC. We do not further discuss mafic ZSTs.

We determined whole-rock Hf isotopic compositions of AIC samples at the Radiogenic Isotope and Geochronology Laboratory (RIGL) at WSU (Pullman, WA) by solution-multi-collector (S-MC) ICP-MS (Table 2) using a ThermoFinnigan Neptune MC-ICP-MS and an Aridus

Table 1 Locations, descriptions, and petrography for samples collected from the Austurhorn intrusive complex

Sample[a]	Location (UTM)[b]		Mafic bodies present?[c]	Mafic relative abundance[d] (%)	Major mineral phases[e]	Accessory mineral phases[f]
	Easting	Northing				
IA-NS-1	524180	7146224	None	0	Qz (~30 %), Afs + Pl (~60 %), Amph (5–7 %), Cpx (~7 %), Bt (<2 %), Alt (<2 %)	FeTi, Zrc, Sph, Ap
IA-NS-2*	524147	7146097	10 cm–1 m	~25	Qz (30–35 %), Afs + Pl (40–45 %), Amph (~10 %), Bt (<1 %), Alt (8–10 %)	FeTi, Zrc, Sph, Ap
IA-NS-3	524101	7145946	>1 m	30–40	Pl (~75 %), Cpx (~10 %), Amph (<5 %), Qz (<5 %), Alt (5–10 %)	FeTi, Zrc, Sph
IA-NS-4a	522153	7144490	1–10 cm	~5	Qz (~30 %), Afs + Pl (~60 %), Amph (<2 %), Bt (<1 %), Alt (<5 %)	FeTi, Zrc, Sph
IA-NS-5	522643	7142846	1 cm–10 m	~70	Qz (~35 %), Afs + Pl (~45 %), Bt (~5 %), Amph (~5 %), Alt (~15 %)	FeTi, Zrc, Sph, Ap
IA-NS-6*	522378	7142211	>1 m	~50	Pl ± Afs (75–80 %), Cpx (~10 %), Qz (~5 %), Alt (10–15 %)	FeTi, Zrc, Sph, Ap
IA-NS-7*	522275	7142118	None	0	Qz (~20 %), Pl + Afs (~45 %), Amph (10–15 %), Bt (5–10 %), Alt (5–10 %)	FeTi, Zrc, Sph
IA-NS-8	522087	7141856	1–10 cm	~5	Qz (~35 %), Pl (~50 %), Alt (~10 %)	FeTi, Zrc, Sph, Ap
IA-G-1*	521924	7142080	n/a	100	Pl (~40 %), FeTi (~10 %), Cpx (~35 %), Amph (<5 %), Qz (<5 %), Alt (<5 %)	Zrc, Sph, Ap
IA-G-3	521149	7142996	n/a	100	Pl (~45 %), Cpx (~30 %), FeTi (15–20 %), Amph (<5 %), Alt (<5 %)	Zr, Ap
IA-G-5*	522402	7142368	n/a	100	Pl (~45 %), FeTi (5–10 %), Cpx (~35 %), Amph (<5 %), Qz (<5 %), Alt (<5 %)	Zrc, Ap, ± Sph

[a] Asterisks denote samples that were processed for zircon extraction

[b] All coordinates were obtained using the World Geodetic System 1984 (WGS 84), Grid 28W

[c] Refers to non-continuous bodies of mafic material surrounded by silicic host (e.g. mafic pillows, enclaves, and clasts); not applicable (n/a) to mafic units

[d] Relative abundance of mafic (vs silicic) material within the outcrop where the sample was collected

[e] Major minerals: *Qz* quartz, *Kfs* alkali feldspar, *Pl* plagioclase feldspar, *Amph* amphibole, *Cpx* clinopyroxene, *Bt* biotite, *Alt* alteration phases

[f] Accessory minerals: *FeTi* Fe–Ti oxides (e.g. magnetite and ilmenite), *Zrc* zircon, *Sph* sphene

desolvating nebulizer for sample introduction (for a more detailed description of preparation procedures and instrument configuration, see supplementary material S1). Mass fractionation was corrected using ^{179}Hf/^{177}Hf $= 0.7325$, and all sample analyses were normalized using the Hf isotope reference material JMC-475 (accepted ^{176}Hf/^{177}Hf $= 0.282160$; Vervoort and Blichert-Toft 1999). Analyses of JMC-475 were done during the course of this study and yield a mean ^{176}Hf/^{177}Hf of 0.282135 ± 7 (2SD; $n = 15$). Present-day $\varepsilon_{\mathrm{Hf}}$ values were calculated using the CHUR parameters reported by Bouvier et al. (2008).

Zircon analyses

We separated individual zircon grains from seven bulk-rock mafic and silicic samples at Vanderbilt University, starting with 1–2 kg of each sample. For all silicic samples, any mafic or intermediate enclaves and clasts present were mechanically removed from the silicic host matrix prior to processing them for whole-rock geochemistry and zircon extraction. We followed standard separation techniques to concentrate zircon grains, including crushing, milling, sieving, density separation by water and heavy liquid (lithium

Table 2 Whole-rock Hf isotope compositions, measured by solution MC-ICP-MS

Sample	^{176}Hf/^{177}Hf	2SE[a]	^{178}Hf/^{177}Hf	2SE[a]	^{180}Hf/^{177}Hf	2SE[a]	ε_{Hf}	2SE
IA-NS-2	0.283140	±7	1.467182	±11	1.886801	±26	12.6	0.3
IA-NS-6	0.283161	±8	1.467184	±16	1.886733	±32	13.3	0.3
IA-NS-7	0.283182	±6	1.467189	±10	1.886814	±16	14.0	0.2
IA-G-1	0.283138	±6	1.467179	±10	1.886861	±21	12.5	0.2
IA-G-5	0.283128	±7	1.467163	±15	1.886663	±22	12.1	0.3

[a] Errors reported as 10^{-6}

heteropolytungstates in water; LST, $\rho \approx 2.8$ g/mL), separation by magnetic susceptibility (Frantz Isodynamic Magnetic Separator), and hand-picking individual zircon grains from the heavy separate fraction under a stereoscope. Separated zircon grains were mounted in epoxy resin, polished to expose interiors, and imaged by reflected light, using a stereoscope. All zircons were then imaged by cathodoluminescence (CL) using either a TESCAN Vega 3 LM variable pressure scanning electron microscope (SEM) at Vanderbilt University or a JEOL JSM 5600 SEM at the Stanford-USGS Micro Analytical Center (SUMAC). Zircon reflected light (RL) and CL images were our primary guides in selecting the location of spots on individual grains for ion microprobe analyses (for detailed zircon CL images and selected spots for analysis, see supplementary figure S2).

We measured zircon trace element concentrations and U–Pb isotopes in situ using the Stanford-USGS sensitive high-resolution ion microprobe with reverse geometry (SHRIMP-RG; for additional details on instrument configuration and analyses, see supplementary material S1). All data were reduced using the Microsoft Excel add-in program Squid2.51 (Ludwig 2009), using Si^{4+} as the internal element for internal calibration. Calculated model U–Pb ages are standardized relative to R33 zircons (419 ± 1 Ma, Black et al. 2004). For consistency across all samples, any analyses that contained high common Pb (>20 %), high or low UO/U (>2 SD from sample mean), or were age outliers (>2 SD from sample mean) were excluded from our calculation of mean U–Pb ages. We report all U–Pb ages for the AIC with 2σ uncertainty, corrected for common lead (^{207}Pb, assuming concordance) and thorium (^{230}Th) disequilibrium using the Th/U ratio of each respective whole-rock sample as the assumed magma value (for full U–Pb isotope data, see Table S2 in supplementary materials). We analyzed a large suite of trace elements, with particular emphasis on Ti for thermometry (see below), and U, Th, Hf, and the rare earth elements (REEs) for evaluating magma evolution and characterizing zircon populations (see Table S3 in supplementary materials). Trace element concentrations were standardized relative to well-characterized, homogeneous zircon standards MAD and MADDER (Barth and Wooden 2010) following methods outlined by Grimes et al. (2007, 2015) and Claiborne et al. (2006, 2010b).

We apply the Ti-in-zircon thermometer of Ferry and Watson (2007) to estimate the range of model crystallization temperatures for AIC zircon grains. Using this method, the accuracy of temperatures relies on having accurate Ti measurements in zircons as well as good constraints for the activity of TiO_2 (rutile saturation: $a_{TiO2} = 1$) and SiO_2 (quartz saturation: $a_{SiO2} = 1$) in the magmas from which zircons grew. Rutile is absent in all Austurhorn rocks, but Fe–Ti oxides (e.g. ilmenite and titanite) are coexisting accessory phases with zircon in most silicic rocks throughout the AIC (see Table 1), so we can reasonably assume that a_{TiO2} was <1 but ≥0.5 during zircon crystallization (e.g. McDowell et al. 2014). Furthermore, while some zircon crystallization may have occurred prior to quartz saturation, high silica concentrations in almost all samples and typical abundance of quartz suggest that zircon crystallization occurred at or near silica saturation ($a_{SiO2} = 1$). We infer that the zircons in the gabbro samples were crystallized in highly evolved melt pockets in which a_{SiO2} was also high, though it is likely that a_{TiO2} was higher and a_{SiO2} lower in gabbros during zircon crystallization than in the silicic units of the AIC. Using these constraints, we assume uniform values of $a_{TiO2} = 0.5$ and $a_{SiO2} = 1.0$ in our estimates of model zircon crystallization temperatures (e.g. McDowell et al. 2014). The external errors (1σ) for Ti concentrations in AIC zircons measured by SHRIMP-RG range from ±2.1 to ±4.8 % (errors decrease with increasing Ti abundance). Assuming uncertainties for a_{SiO2} and a_{TiO2} are on the order of ±0.05 and ±0.1, respectively, these external errors introduce propagated uncertainties on the order of ±25–44 °C to the model crystallization temperatures (see Table S3; for Ti-in-zircon thermometry error calculations, see Table S4).

Recent work by Ghiorso and Gualda (2013) suggests a likely range of a_{TiO2} for silicic magmas of 0.3–0.9. They infer that a_{TiO2} increases systematically with decreasing temperature during crystallization of silicic magmas (rhyolite and dacite) such that the difference between the maximum and minimum model Ti-in-zircon temperatures is likely to be an underestimate of the true range of crystallization temperatures. For melts saturated in Fe–Ti oxide phases, a_{TiO2} is unlikely to vary substantially during crystallization (by more than a few tenths), thus allowing us to hold a_{TiO2} constant in our calculations and make comparisons between model Ti-in-zircon crystallization temperatures, as well as identify any statistically significant temperature fluctuations (ΔT > 200–300 °C) in the lifetime of a magma or magmatic system as recorded by zircons (Ghiorso and Gualda 2013; see also Claiborne et al. 2006; Pamukcu et al. 2013; McDowell et al. 2014).

We measured oxygen isotopic ratios on individual spots in zircons by secondary ion mass spectrometry (SIMS) in dual Faraday cup multi-collection mode using the CAMECA IMS1270 ion microprobe at the University of California-Los Angeles (UCLA) W.M. Keck Foundation Center for Isotope Geochemistry (Los Angeles, CA), following the methods outlined by Trail et al. (2007) (for additional details on instrument configuration, see supplementary material S1). We used reference material R33 zircons ($\delta^{18}O = 5.55 \pm 0.08$ ‰, 2SD, Valley 2003) to correct for instrumental mass fractionation. The reproducibility of R33 for all sessions combined was ±0.6 ‰ (2SD; $n = 139$), in agreement with published laser fluorination compositions for R33 zircons (Valley 2003). We omitted 13 individual analyses with $\delta^{18}O$ outside 2SD from the mean, including two reproducible analyses from one R33 grain with ~0.7 ‰ higher $\delta^{18}O$ and three from one grain with ~0.8 ‰ lower than the accepted value. Oxygen isotope data are reported in the $\delta^{18}O$ notation relative to Vienna Standard Mean Ocean Water (VSMOW), with 2σ uncertainties (calculated in quadrature using both the analytical uncertainty of individual analyses and the external reproducibility of standards), in Table S5 in supplementary materials.

The Lu–Hf isotopic compositions of AIC zircons were measured in situ at Memorial University of Newfoundland (MUN) Micro Analysis Facility (MAF-IIC; St. John's, Canada) and the Radiogenic Isotope and Geochronology Laboratory (RIGL) at WSU by laser ablation-multi-collector (LA-MC) ICP-MS. Analyses done at MUN used a ThermoFinnigan Neptune MC-ICP-MS interfaced to a Geolas Pro 193 nm Ar–F excimer laser following the methods of Fisher et al. (2011), with the exception that N_2 was added to the carrier gas for increased sensitivity. Analyses done at WSU used a ThermoFinnigan Neptune MC-ICP-MS interfaced to a New Wave 213 nm Nd-YAG laser and followed the methods outlined by Fisher et al. (2014), with the exception that U–Pb ages were not simultaneously determined (additional details on instrument configuration for both labs can be found in supplementary material S1). We used standard reference material Mud Tank zircons ($^{176}Hf/^{177}Hf = 0.282507 \pm 6$, Woodhead and Hergt 2005) to normalize all samples at WSU. All analyses combined yield a $^{176}Hf/^{177}Hf$ of 0.282507 ± 20 (2SD; $n = 32$), in agreement with the published isotopic composition of Mud Tank zircons. Analyses conducted at MUN did not require correction to an external standard since measured values matched the accepted reference values within error. Secondary reference zircon samples FC-1, MUNZirc 2 and MUNZirc 4, and GJ-1, analyzed interspersed with unknowns at both MUN and WSU, agree well (within 1 SD) with published S-MC-ICPMS isotope compositions of purified Hf from these zircon samples (see supplementary material S1). Present-day ε_{Hf} values were calculated using the CHUR parameters reported by Bouvier et al. (2008). Laser Lu–Hf isotopic data are presented with 2SE uncertainty in Table S6 in supplementary materials.

Results

Field observations

The main focus of our study is to use zircons to quantify the complex magmatic processes indicated by exposures of the mafic–silicic composite zone in the AIC. We recognize two types of mafic enclaves found throughout the MSCZ (Fig. 3): pillow shapes and clasts. Pillows are light to dark gray masses ranging in size from a few centimeters to meters in the long dimension. We interpret these to represent melt-rich mafic magma enclosed by silicic magma. Their margins are commonly cuspate or crenulated, sometimes chilled, and diffuse boundaries are also present. Double pillows or "pillows within other pillows" (see Mattson et al. 1986), usually a chilled dark mafic pillow surrounded by a lighter intermediate gradational outer zone, which is commonly also chilled, all surrounded by the host silicic rock, are also present throughout the MSCZ (e.g. Fig. 3d). Some large pillows are disaggregated into smaller enclaves (clasts) at the margins. Clasts have the same range in size as pillows but are typically darker in color and finer-grained with sharp and angular edges (see Fig. 3a, b, d, e). We interpret clasts to represent fragments of solidified mafic magma within silicic magma. Some enclaves are partially bounded by angular edges and partially by diffuse or crenulated margins.

In addition to mafic enclaves (both pillows and clasts), there are large uniform bodies of fine-grained, homogeneous mafic rock within the MSCZ that have a sill-like morphology (Fig. 3h, i), a feature also recognized by Furman et al. (1992a). The edges of these sill-like bodies are commonly disaggregated into mafic clasts with veins of silicic material intruding as apophyses (e.g. Fig. 3c). In some locations, we find wide areas of clast- and pillow-free silicic rock between mafic sills. Groups of small mafic clasts are often concentrated along the edges of sills and can be reconstructed in the manner of a jigsaw puzzle into the larger structures from which they disaggregated, indicating they were not transported very far by the host magma (e.g. <10 s of cm).

Silicic rocks in the MSCZ are typically fine-grained and can be grouped into general "units" based on distinctive characteristics that extend over 10 s of meters (or more) of outcrop. These units range in appearance from very large, homogeneous, and clast- and pillow-free bodies to extensively mingled composite bodies of silicic material with abundant mafic clasts and pillows of all types and sizes (see above for types; sizes range from cm to m-wide bodies). We refer to the latter as heterogeneous silicic units. These units commonly contain microenclaves (<1 cm across) with gradational contacts and generally becoming more mafic in composition than the host rock toward the center of the enclave. This thoroughly diffuse character is typically interpreted to represent magmatic hybridization (see Fig. 3e; e.g. Vernon 1984; Wiebe et al. 2002; Weidendorfer et al. 2014). Miarolitic cavities are common in most silicic units, indicating that they reached water saturation during the last stages of solidification. Some of the less silicic rocks contain distinctive acicular amphibole crystals and are generally clast-free and pillow-free.

Near the structural top of the MSCZ (below the contact with Hvalnesfjall gabbro, at the base of Hvasshjalli peak; see Fig. 2), there is a zone of nearly enclave-free granophyre that is widely intruded by small-volume dikes and pods of high-SiO_2 granophyre (>75 wt% SiO_2). These high-SiO_2 granophyre units are volumetrically insignificant relative to the rest of the rocks in the MSCZ, making up $\ll$1 % of exposed silicic rocks. Their geochemical characteristics differ significantly from those of other associated silicic rocks, suggesting that they were formed by different, smaller-scale magmatic processes (e.g. extreme differentiation and in situ melting) that were likely not widespread in the AIC (Padilla 2015). Because of their magmatic association with other units of the MSCZ, we include four samples from this high-SiO_2 granophyre zone in our U–Pb zircon age determination for the entire Austurhorn complex (samples IA-NS-4b, IA-NS-9, IA-NS-10, and IA-NS-12; see U–Pb results, in "Zircon results" section) in order to maximize the age resolution. However, these samples are the subject of a separate study (see Padilla 2015) and are therefore not discussed further here.

A zone of homogeneous fine-grained granophyre, free of mafic enclaves and clasts, surrounds the MSCZ. This granophyre intrudes the country rock basalts marking the northern boundary of the AIC. In a few locations, the MSCZ is also in contact with the coarse-grained Hvalnesfjall gabbro (sample IA-G-3; see Fig. 2; Furman et al. 1992a). A small body of gabbro that we refer to as the "coastal" gabbro is exposed within the MSCZ at Hvalneskrókur Point (Fig. 2). Unlike the mafic sheets elsewhere in the MSCZ, the coastal gabbro (sample locality IA-G-1) is coarse-grained and gradational with the surrounding silicic units. Dikes, apophyses, and thin veins of silicic rock intruded into the coastal gabbro. We refer to all other gabbroic units within the MSCZ as "sheet" gabbros (e.g. sample IA-G-5).

Petrography

All silicic and intermediate samples from the MSCZ display micrographic intergrowths of quartz and feldspar. Individual large (dominantly plagioclase) feldspar crystals and quartz ranging from ~500 to ~1000 μm across are also present and common in the sample matrix (see supplementary figure S1). In addition, minor amounts of prismatic clinopyroxene and amphibole are present in most silicic samples, and zircon and titanite are common accessory minerals in all units. One heterogeneous granophyre sample (IA-NS-2) contains abundant microenclaves with diffuse boundaries and abundant large (>1 cm in length) amphibole crystals.

All sampled gabbros share the same mineral assemblage, composed mainly of very large plagioclase and clinopyroxene (1–2 cm across), as well as Fe–Ti oxides, and minor amounts of biotite. Amphibole is also present, though typically as a secondary phase. Some Fe–Ti oxides from the coastal gabbro (sample IA-G-1) display an acicular habit, a feature that is absent in the sheet gabbros of the MSCZ. The Hvalnesfjall gabbro (IA-G-3) is distinctively coarser than all MSCZ gabbros and displays the least alteration.

A small proportion of amphibole crystals, particularly in the intermediate and silicic samples, are fibrous and often contain cores of patchy primary clinopyroxene. We interpret these crystals to be secondary amphibole crystallization replacing primary clinopyroxene as a result of sub-solidus hydrothermal alteration (e.g. Veblem and Buseck 1981; Furman et al. 1992b). Most samples (of all compositions) contain other secondary phases such as epidote, chlorite, and sericite in minor amounts, also indicating that some sub-solidus alteration has occurred throughout the AIC.

Whole-rock geochemistry

Of the eleven analyzed samples, three are representative of gabbroic rocks present throughout the AIC (the coastal and sheet gabbros within the MSCZ, and the adjacent Hvalnesfjall gabbro). The rest encompass the range of silicic compositions and textures that are most common within the MSCZ, and the homogeneous granophyre zone that surrounds the MSCZ.

All samples are metaluminous and have tholeiitic affinities (high FeO/(FeO + MgO) and other trace element characteristics). Silicic and intermediate samples range in SiO_2 concentrations from 61 to 73 wt% and display oxide versus SiO_2 trends that are typical of silicic rocks (see supplementary material S2). The mafic samples are all near 47 wt%, but differ significantly from each other in their elemental abundances. The Hvalnesfjall gabbro (sample IA-G-3) is chemically similar to the sheet gabbro in the MSCZ (IA-G-5), both being more cumulate-like in character relative to the coastal gabbro (IA-G-1), which is distinctly more evolved and reflects a fractionated tholeiitic melt.

Measured Hf isotopic compositions of AIC whole-rock samples range from +12 to +14 $\varepsilon_{\mathrm{Hf}}$ (Table 2). The gabbro samples and the granophyre define the lower range of isotope compositions at +12.1 ± 0.3 (sheet gabbro IA-G-5), +12.5 ± 0.2 (coastal gabbro IA-G-1), and +12.6 ± 0.3 $\varepsilon_{\mathrm{Hf}}$ (granophyre IA-NS-2). The intermediate units both have slightly higher $\varepsilon_{\mathrm{Hf}}$ compositions at +13.3 ± 0.3 (diorite IA-NS-6) and +14.0 ± 0.2 (granodiorite IA-NS-7).

Zircon results

We extracted zircons from five MSCZ samples for in situ elemental geochemistry, U–Pb geochronology, and O and Hf isotopic analyses. As previously noted ("Zircon results" section), we also report ages for an additional four related samples, but only discuss the five samples that are volumetrically significant and therefore representative of widespread magmatic processes in the MSCZ. The silicic samples encompass the range of textures and rock types found within the MSCZ: a heterogeneous granophyre (IA-NS-2) that contains all mafic enclave types and displays extensive interactions between mafic input and silicic host; a homogeneous, fine-grained diorite (IA-NS-6) that hosts abundant mafic enclaves, both large, diffuse pillows and smaller angular clasts; and a homogeneous, medium-grained and enclave-free micrographic granodiorite (IA-NS-7) characterized by abundant acicular amphibole crystals. The selected mafic samples are from relatively homogeneous and voluminous exposures of gabbro within the MSCZ and include the coarse-grained coastal gabbro (IA-G-1) and a finer-grained sheet gabbro from the interior of the MSCZ (IA-G-5).

A simple qualitative assessment of zircon yields from Icelandic silicic volcanic rocks (e.g. Carley et al. 2011), and MSCZ rocks reveal that zircons are significantly more abundant in intrusive rocks than in volcanic rocks. Carley et al. (2011) report that zircon populations in seven samples from different silicic volcanic systems were sparse (typically 10 s of grains/kg of starting whole-rock material). In contrast, we find that every MSCZ rock, including gabbros and samples of intermediate compositions, yields abundant zircons (≫100 grains/kg, except for the sheet gabbro, IA-G-5, which yielded ~20 grains/kg).

Grain morphology and zoning patterns vary widely throughout all MSCZ zircon samples, including complex growth, patchy, sectoral, and simple zoning. Growth-zoned euhedral and prismatic crystals, ranging from acicular (6:1 aspect ratio) to subequant (1:1 aspect ratio), are common in all MSCZ rock types, though slightly rounded grains are also present in all samples (Fig. 4). Crystals generally range from ~50 to ~300 µm in length (on the long axis) for all units, but in some samples (e.g. coarse gabbro) the largest grains can be up to ~500 µm in length. A small number of grains preserve evidence of resorption and subsequent crystallization events in the form of irregular cores with truncated internal zoning surrounded by prismatic zircon overgrowth (Fig. 4).

The heterogeneous granophyre (IA-NS-2) has the highest proportion of growth-zoned euhedral crystals, although there is a small proportion of grains that contain simple zoning (characterized by broad bands that appear homogeneous in CL intensity; see Fig. 4) and resemble zircon grains from Icelandic volcanic rocks (Carley et al. 2011). Crystals in the intermediate samples (IA-NS-6 and IA-NS-7) display the greatest amount of rounding and resorption, and a large proportion of grains from the diorite (IA-NS-6) are anhedral (Fig. 4).

Zircon grains from the coastal gabbro (IA-G-1) are larger than those from silicic samples, and they display diverse internal structures, including growth, sector, and patchy zoning (characterized by irregular and discontinuous patches of high CL intensity) and interiors that lack visible zoning (Fig. 4). In contrast, zircons from the sheet MSCZ gabbro (IA-G-5) are typically small, generally exhibiting euhedral crystal shapes, bright in CL intensity, and commonly either sector-zoned or lacking visible zoning in CL (see Fig. 4). For each sample, we targeted both rim and interior zones, including cores, during zircon trace element analyses so as to document any geochemical differences between earlier and later stages of zircon growth.

The elemental compositions of most AIC zircon grains are generally consistent with what has been observed for zircons from other Icelandic silicic rocks (Fig. 5; Carley et al. 2011, 2014). Uranium and thorium abundances range from ~50 to ~6000 ppm and ~15 to ~5000 ppm, respectively (Fig. 5). Despite this wide range of concentrations, they form a well-defined array with a Th/U ratio that varies systematically from ~0.5 to ~2 with increasing U and Th. Hafnium concentrations are mainly between ~6000 and ~12,000 ppm (Fig. 5), and Ti abundances range from ~5 to ~40 ppm in all samples, similar to those in other Icelandic zircons (Carley et al. 2011, 2014). We also observe a general trend of decreasing Ti with increasing Hf concentrations, as is documented in other co-genetic zircon populations (e.g. Claiborne et al. 2006). A majority of zircons from mafic samples, particularly the coastal gabbro (IA-G-1), have some elemental signatures that differ from the silicic array, most noticeably lower Nb concentrations and higher Eu/Eu* (Fig. 5).

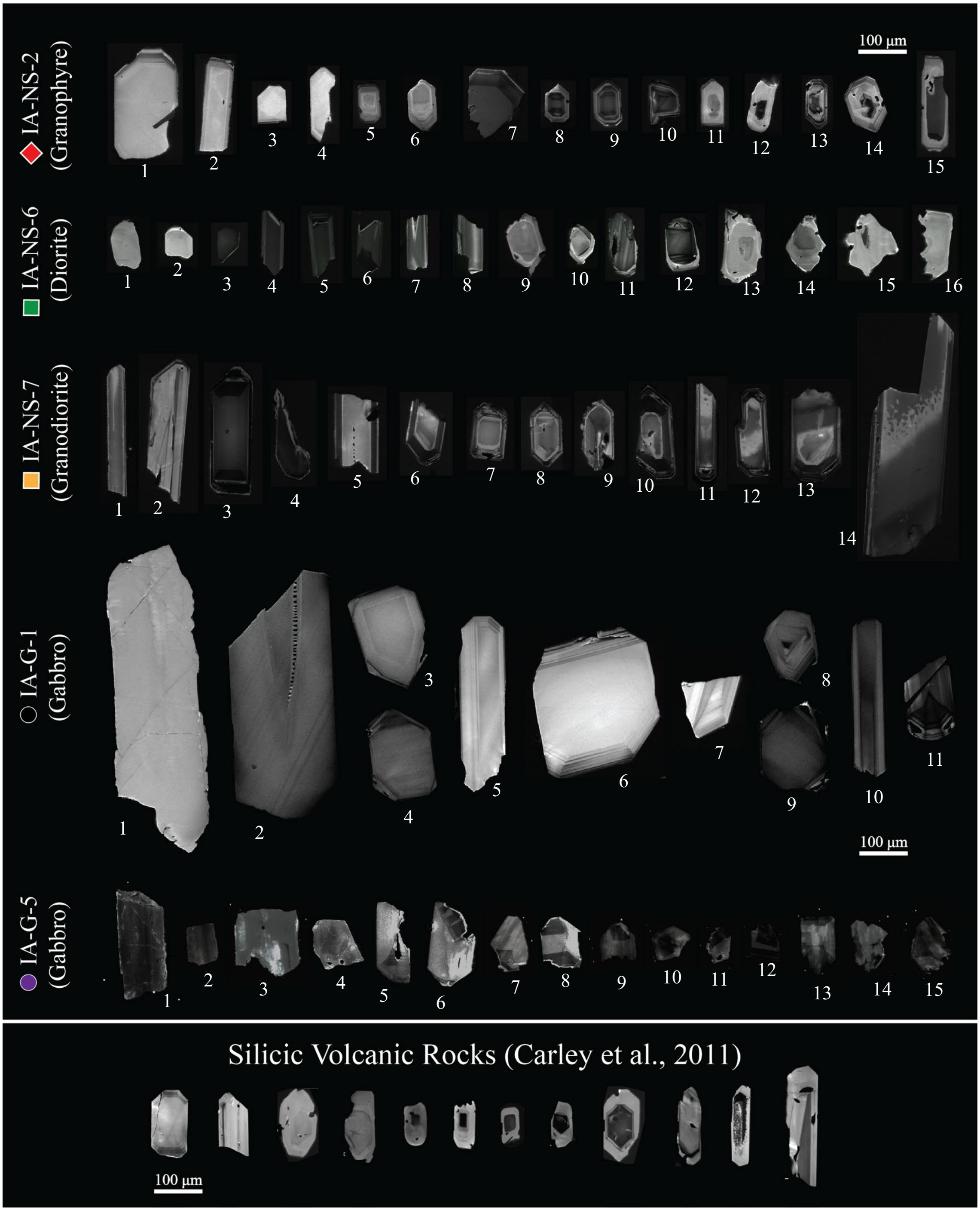

Fig. 4 SEM cathodoluminescence images of representative zircon from AIC rocks. *Granophyre*: morphologies include large (*1*, *7*) and small (*6*, *8–11*) euhedral, acicular (*2*, *15*), and slightly rounded (*12*, *15*) grains; zoning includes simple (*1–7*), oscillatory (*8–10*), and some anhedrally shaped cores surrounded by zircon overgrowth (*11–15*). *Diorite*: morphologies include rounded (*1–2*, *9–12*), acicular (*4–8*), and anhedral (*13–16*) grains; zoning includes simple/unzoned (*1–3*), sector (*4–8*, *12*), striped (*3*, *5–6*), and oscillatory (*10*, *14*), and anhedrally shaped cores surrounded by zircon overgrowth are common (*9–13*), sometimes containing multiple anhedral zones (*13*). *Granodiorite*: morphologies include mainly acicular (*1–5*, *11–14*), and small euhedral (*6–10*) grains, some with slightly resorbed/rounded edges (*2*, *4*, *7*, *9–10*, *13*); zoning includes sector (*3*), simple (*1–2*, *4*, *14*), and oscillatory (*5–13*). *Coastal Gabbro*: grains are generally larger than those from silicic units; morphologies include acicular (*1–2*, *5*, *10*), euhedral (*3–4*, *6–9*, *11*), and occasionally resorbed (*1*) grains; zoning includes simple (*1–3*, *9*), sector (*10–11*), and oscillatory (*5–8*, *11*). *Sheet Gabbro*: morphologies include acicular (*1*, *5*), small euhedral (*6–9*), and rounded/resorbed (*2–4*, *11–15*) grains; zoning includes CL-dark and simple (*1–4*, *10–15*), sector (*6*, *8–9*), and occasionally oscillatory (*7*)

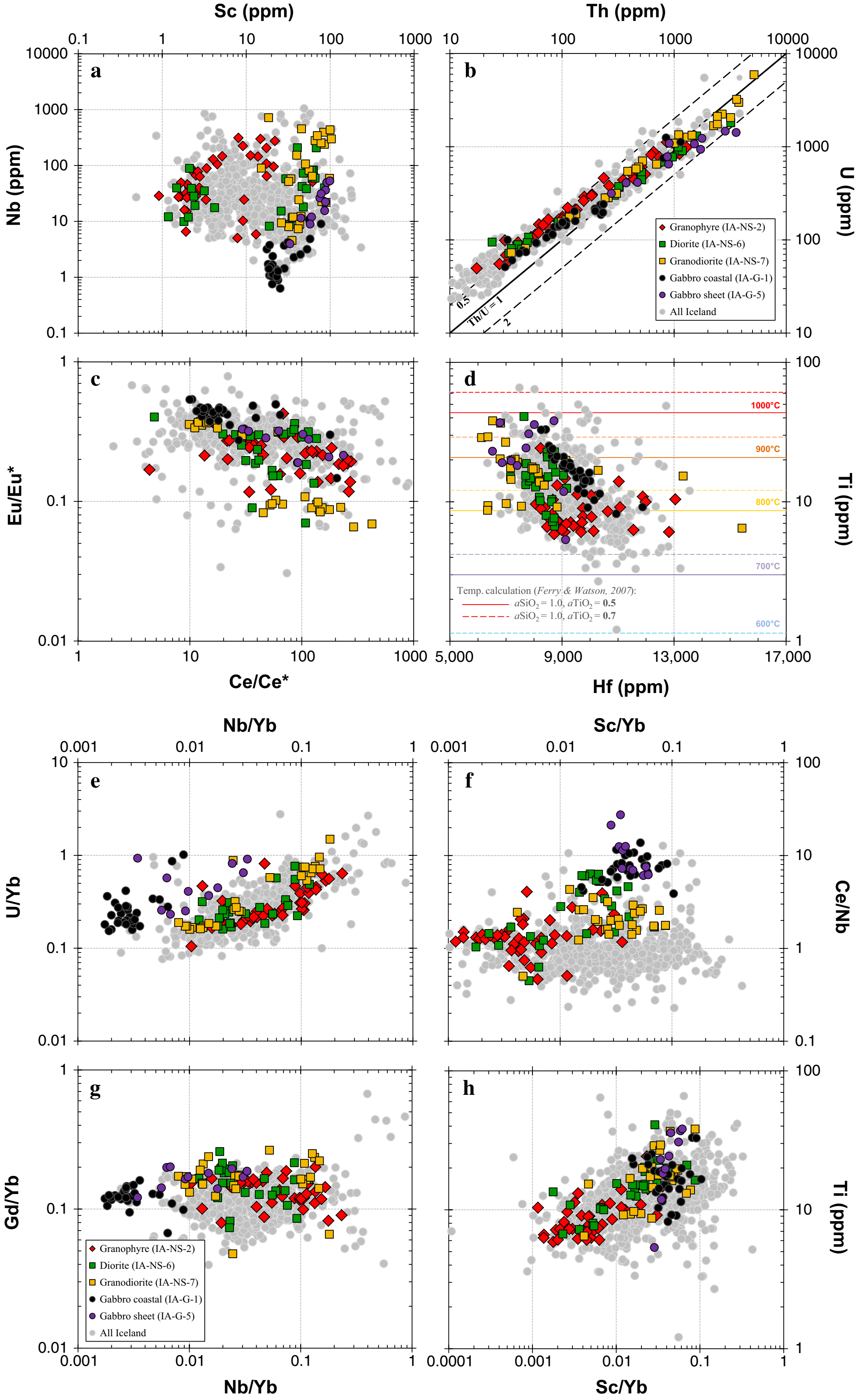
a
Sc (ppm)
0.1
1
10
100
1000
Nb (ppm)
10000
1000
100
10
1
0.1
b
Th (ppm)
10
100
1000
10000
U (ppm)
10000
1000
100
10
0.5
Th/U = 1
2
Granophyre (IA-NS-2)
Diorite (IA-NS-6)
Granodiorite (IA-NS-7)
Gabbro coastal (IA-G-1)
Gabbro sheet (IA-G-5)
All Iceland
c
Eu/Eu*
1
0.1
0.01
Ce/Ce*
1
10
100
1000
d
Ti (ppm)
100
10
1
1000°C
900°C
800°C
700°C
600°C
Temp. calculation (Ferry & Watson, 2007):
aSiO2 = 1.0, aTiO2 = 0.5
aSiO2 = 1.0, aTiO2 = 0.7
Hf (ppm)
5,000
9,000
13,000
17,000
e
Nb/Yb
0.001
0.01
0.1
1
U/Yb
10
1
0.1
0.01
f
Sc/Yb
0.001
0.01
0.1
1
Ce/Nb
100
10
1
0.1
g
Gd/Yb
1
0.1
0.01
Nb/Yb
0.001
0.01
0.1
1
Granophyre (IA-NS-2)
Diorite (IA-NS-6)
Granodiorite (IA-NS-7)
Gabbro coastal (IA-G-1)
Gabbro sheet (IA-G-5)
All Iceland
h
Ti (ppm)
100
10
1
Sc/Yb
0.0001
0.001
0.01
0.1
1

◂ **Fig. 5** Trace element abundances and ratios for zircon from the AIC. "*All Iceland*" group (gray symbols) from Carley et al. (2014; includes Icelandic zircon data from volcanic, plutonic, and detrital samples) plotted for comparison. **a** Sc (ppm) versus Nb (ppm); **b** Th (ppm) versus U (ppm); the *solid line* indicates a Th/U ratio of 1; the *dashed lines* indicate Th/U ratios of 0.5 (top) and 2 (bottom); **c** Ce/Ce* (Ce anomaly) versus Eu/Eu* (Eu anomaly); **d** Hf (ppm) versus Ti (ppm); the *colored lines* indicate Ti-correlated zircon crystallization temperatures, calculated using the Ti-in-zircon thermometer of Ferry and Watson (2007); **e** Nb/Yb versus U/Yb; **f** Sc/Yb versus Ce/Nb; **g** Nb/Yb versus Gd/Yb; **h** Sc/Yb versus Ti (ppm)

With few exceptions, all zircons from the AIC have REE patterns that display chondrite-normalized trends of extreme enrichment in heavy rare earth elements (HREEs) relative to light rare earth elements (LREEs) and positive Ce and negative Eu anomalies (Fig. 6). A few zircon analyses from the heterogeneous granophyre (IA-NS-2) and the diorite (IA-NS-6) show anomalous LREE enrichment. These are probably the result of encountering LREE-rich inclusions, such as glass or minerals that concentrate

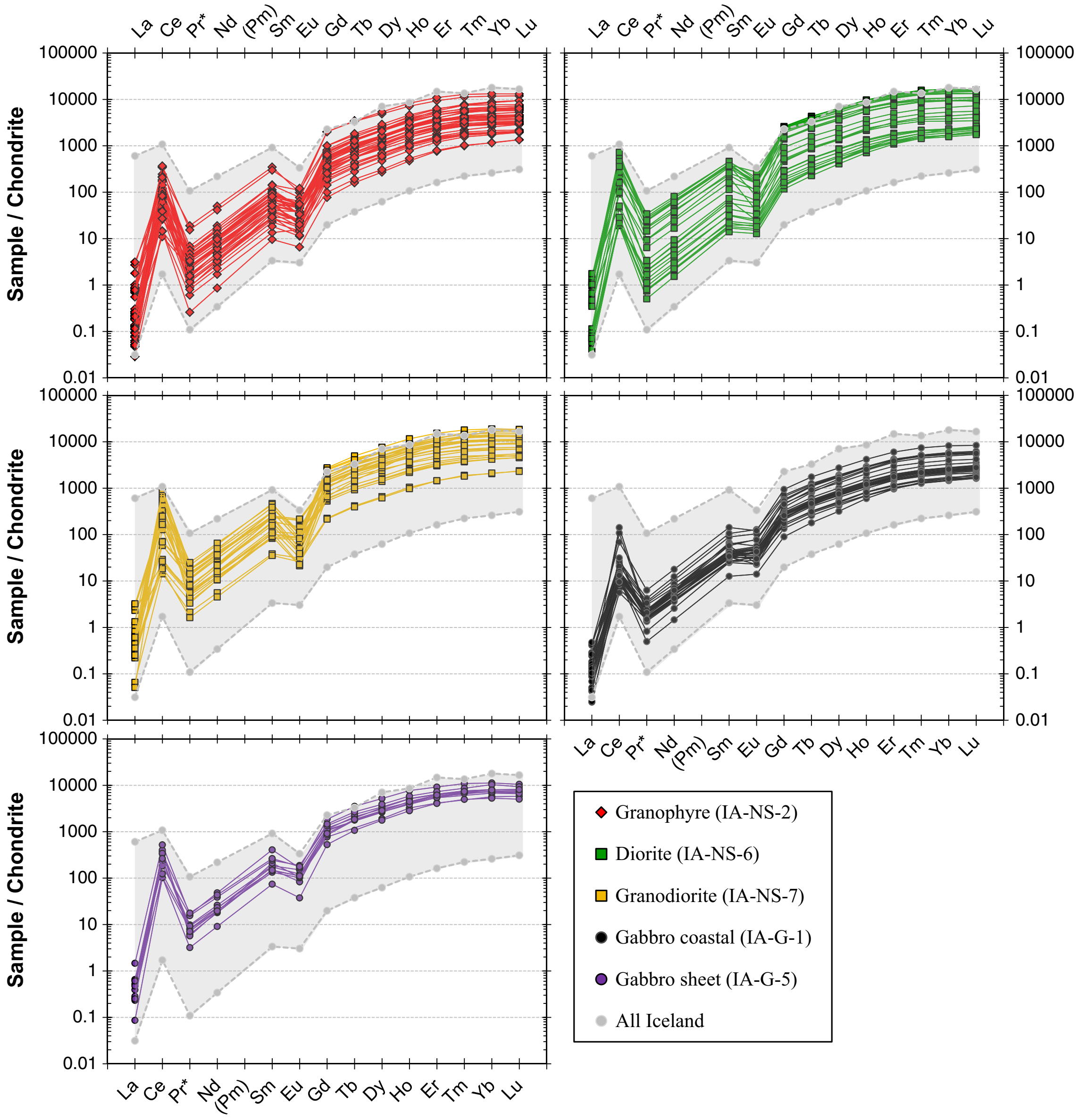

Fig. 6 Chondrite-normalized zircon rare earth element (REE) abundances in samples from the AIC. The *gray shadow* in each individual sample plot represents the range of REE abundances found in zircon from other analyzed volcanic, plutonic, and detrital Icelandic samples (see Carley et al. 2014), plotted for comparison to AIC zircon

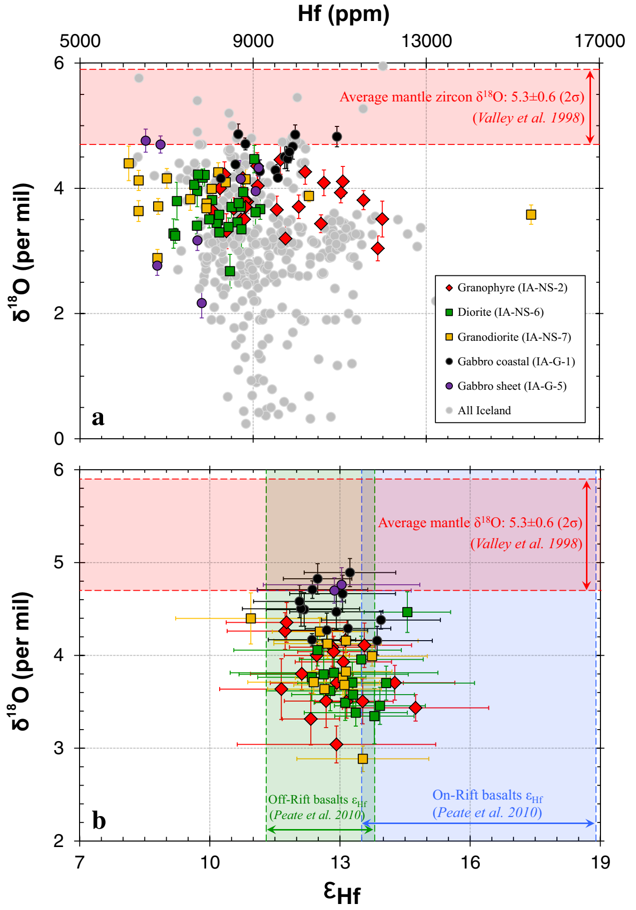

Fig. 7 Isotopic compositions of zircon grains from the AIC. All errors are plotted as 2σ. **a** Hf (ppm) versus δ^{18}O; the *red zone* indicates the measured δ^{18}*Orange* of mantle zircon (+5.3 ± 0.6 ‰, Valley et al. 1998). **b** $\varepsilon_{\mathrm{Hf}}$ versus δ^{18}O; the *blue zone* indicates the range of Hf isotopic compositions of Icelandic *on-rift* basalts (from the Northern and Western Volcanic Zones; Peate et al. 2010); the *green zone* indicates the range of Hf isotopic compositions of Icelandic *off-rift* basalts (from the Eastern Volcanic Zone, Snæfellsnes Peninsula, Vestmannæyjar, and Snæfell volcano; Peate et al. 2010)

LREE (e.g. chevkinite and allanite), during analyses, and are omitted from our plots.

Oxygen isotopic values (δ^{18}O) for AIC zircons range from +2.2 to +4.8 ‰. All δ^{18}O values are depleted relative to zircon mantle values (+5.3 ± 0.6 ‰, 2σ; Valley et al. 1998). Mean δ^{18}O for individual silicic samples are indistinguishable within error (Fig. 7a): +3.8 ± 0.7 ‰ (all uncertainties are 2σ) for the granophyre (IA-NS-2), +3.7 ± 0.8 ‰ for the diorite (IA-NS-6), and +3.9 ± 0.7 ‰ for the granodiorite (IA-NS-7). The gabbros show oxygen values that are distinct from one another, with the coastal gabbro (IA-G-1) being the most reproducible and having the highest mean δ^{18}O (+4.5 ± 0.5 ‰) and the sheet gabbro (IA-G-5) displaying the largest variability of any of the samples (from +2.2 to +4.8 ‰, with a mean of +3.8 ± 1.8 ‰; Fig. 7a).

Measured hafnium isotope ratios (reported as $\varepsilon_{\mathrm{Hf}}$) for zircons from analyzed samples range from +11 to +16 ε-units (average 2SE for individual analyses is ~1.3 ε-units). When all units are pooled together, they yield a population weighted mean of +13.0 ± 0.2 ε-units (2σ, $n = 74$, MSWD = 2.0; Fig. 7b).

Weighted mean zircon U–Pb ages span a range of approximately 320 kyr (Fig. 8). The uncertainty for individual analyses is on average 9.8 %, but the precision generally decreases with increasing U concentration and/or common Pb. The gabbros and high-SiO$_2$ granophyre zone samples make up the older part of this range (granophyres: IA-NS-4b, 6.67 ± 0.06 Ma [all uncertainties are 2σ SE]; IA-NS-9, 6.53 ± 0.07 Ma; IA-NS-10, 6.57 ± 0.24 Ma; IA-NS-12, 6.61 ± 0.22 Ma; sheet gabbro IA-G-5, 6.56 ± 0.05 Ma; and coastal gabbro IA-G-1, 6.42 ± 0.09 Ma). The younger ages are for granophyre IA-NS-2 (6.40 ± 0.12 Ma), granodiorite IA-NS-7 (6.36 ± 0.08 Ma), and diorite IA-NS-6 (6.35 ± 0.08 Ma). All zircon data when pooled yield a mean age of 6.52 ± 0.03 Ma (MSWD = 1.8, $n = 137$, 25 rejected; see Fig. 8).

Discussion

Field interpretations

Evidence for open-system processes, such as repeated mafic magmatic replenishment, is ubiquitous within the MSCZ in the AIC (Fig. 3). The contacts between different silicic rock units within the MSCZ are typically gradational. They are primarily identified by an increase or decrease in the amount and type of mafic material present (e.g. abundant small clasts versus large pillows or sheets) or observable changes in texture. In some locations, contacts between units are identified by changes in mineral assemblage (e.g. the presence of acicular amphiboles, or abundance of Fe–Ti oxides). Crenulated and chilled margins on some mafic enclaves indicate that they were a product of fluid–fluid magmatic interactions with the silicic host (i.e., both magmas behaved fluidly during their interaction so as to produce the observed textures). Furthermore, enclaves with both angular and crenulated margins against the same silicic host rock suggest that quenched pillows can subsequently fracture within the same host magma after intrusion. This indicates that the host silicic magma remained mobile after the mafic magma solidified. In some areas of the MSCZ, large sheet-like mafic bodies are preserved, and their edges are commonly disaggregated into enclaves and clasts within the surrounding silicic rock (see Fig. 3h, i). A common form of mafic recharge into the system may be through intrusion of mafic sheets that disaggregate into the host magma (e.g. Wiebe and Collins 1998; Harper et al.

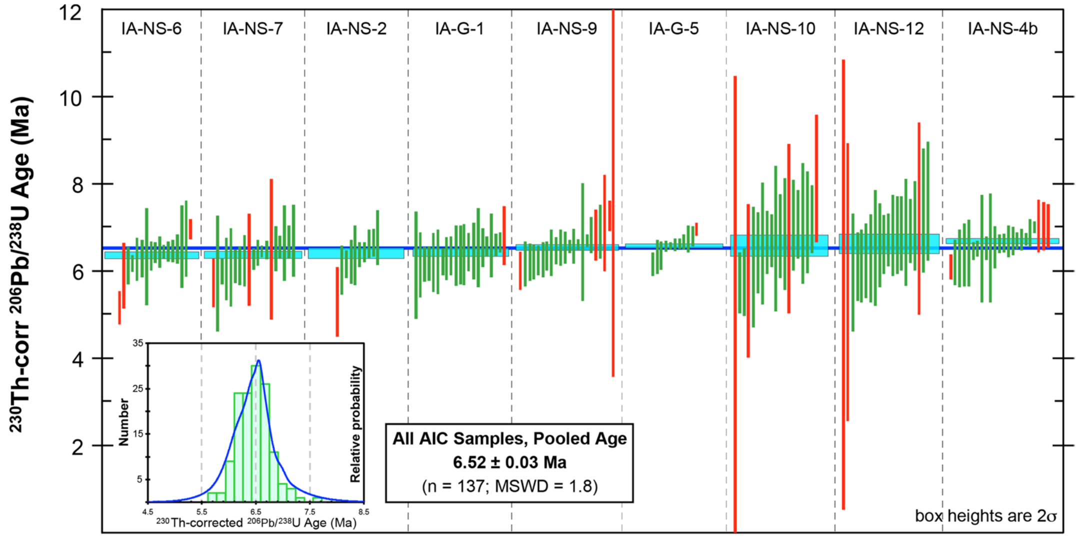

	IA-NS-6	IA-NS-7	IA-NS-2	IA-G-1	IA-NS-9	IA-G-5	IA-NS-10	IA-NS-12	IA-NS-4b
Wt. Mean Age (Ma):	**6.35 ± 0.08**	**6.36 ± 0.08**	**6.40 ± 0.12**	**6.42 ± 0.09**	**6.53 ± 0.07**	**6.56 ± 0.05**	**6.57 ± 0.24**	**6.61 ± 0.22**	**6.67 ± 0.06**
n:	14	16	9	20	17	10	15	17	19
MSWD:	0.78	1.4	1.3	0.81	1.5	2.2	1.3	0.68	2.3
Rejected analyses:	3	3	1	1	5	1	4	3	4

Fig. 8 Zircon ^{206}Pb/^{238}Pb ages for MSCZ units from the AIC, corrected for initial ^{238}U–^{230}Th disequilibrium. Each *green bar* represents a single zircon age (*bar* height = 2σ SE). *Red bars* represent discarded analyses. For consistency across all samples, any analyses that were either age outliers (>2 SD from sample mean), contained high common Pb (>20 %), or contained high or low UO/U (>2 SD from sample mean), were excluded from our calculation of mean ages. For each sample, the weighted mean age is plotted as a light blue *horizontal box* (height = 2σ SE). The *dark blue line* represents the pooled population age for the entire AIC (6.52 ± 0.03 Ma). The range in mean individual unit ages suggests a timescale of peak magmatic construction of the AIC of ~320 kyr. *Inset:* Probability density distribution and histogram for all AIC zircon ages in this study ($n = 137$)

2004; Wiebe et al. 2004; Weidendorfer et al. 2014). Areas of what we interpret to be remobilized silicic material are often intermingled extensively with voluminous mafic rock, also indicative of magma replenishment events.

We interpret the field relationships to indicate a mush-like environment for the AIC in which the partially solidified silicic host material was continually reheated, revived, and remobilized within the MSCZ by the repeated intrusion of hotter mafic magmas. These mafic intrusions provided the new heat and energy necessary to prolong the longevity of the Austurhorn magmatic system (e.g. Claiborne et al. 2010a).

Zircon abundance, size, and morphology

Zircons from silicic volcanic rocks from Holocene Icelandic eruptions record relatively brief (10 s of kyr), high-temperature histories that reflect magmatic conditions just prior to, and leading up to, eruptive events (Carley et al. 2011, 2014). These volcanic rocks are rich in Zr (mostly ~600 to ~800 ppm; Carley et al. 2011), yet zircons are sparse. In contrast, we found that both mafic and silicic rocks from the MSCZ at Austurhorn contain a vast abundance of zircons, generally larger and with more complex zoning (see Fig. 4). These MFCZ intrusive zircons likely record slow and complete crystallization of their parent magmas. The contrast in relative abundance, size, and complexity of zoning between intrusive and extrusive zircons suggests that most Icelandic zircons are stored and preserved within the rocks of silicic intrusive complexes, rather than in erupted products. The types of complex morphology and zoning features observed in many AIC zircons (Fig. 4) have, in other systems, been interpreted to indicate thermal and chemical fluctuations of the melt within an open and dynamic system during the time of zircon crystallization (Hoskin and Schaltegger 2003; Corfu et al. 2003; Claiborne et al. 2006, 2010b).

Zircon elemental and isotopic compositions

Building on the work of Grimes et al. (2007, 2015), Carley et al. (2014) identified compositional fields for zircon formed in silicic rocks from a range of tectonic–magmatic settings, based on the abundance of Hf, U, REE, Th/U, and Ti-in-zircons (Fig. 9). When plotted on these fields, the Hf composition of AIC zircon crystals fall within the lower extreme (<12,000 ppm) for zircons in continental-type environments. Abundances and ratios of incompatible elements in zircon show that AIC silicic magmas, and Icelandic silicic magmas in general, are less evolved relative

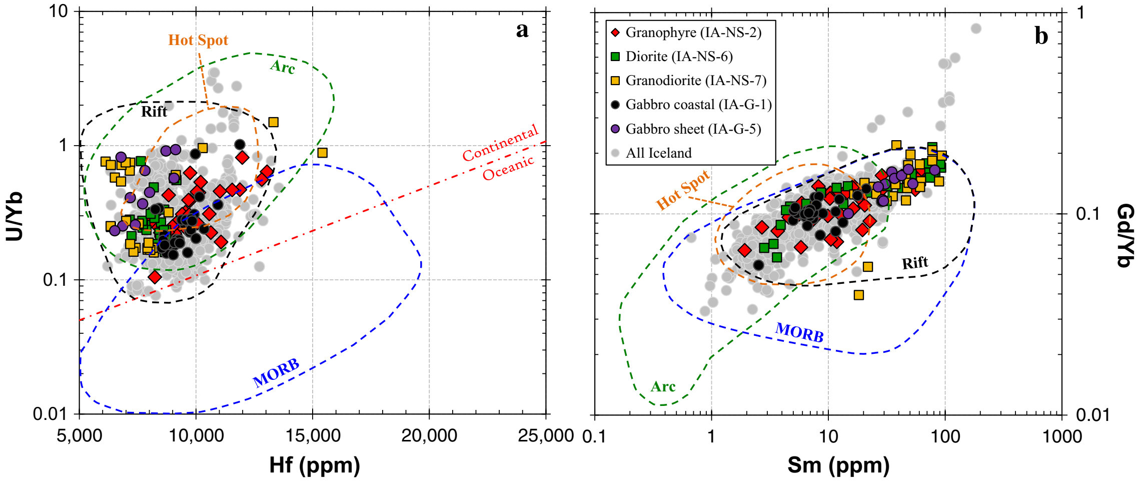

Fig. 9 Discrimination plots for zircon from different tectonic settings (e.g. Grimes et al. 2007) based on trace element geochemistry. The *dashed regions* represent the range of zircon geochemistry for different tectonic settings from around the world (modified after Carley et al. 2014): *blue* Mid-Ocean Ridge Basalt (MORB); *black* evolving continental rift (Alid, E. Africa; Salton Sea, N. America); *orange* continental hot spot (Yellowstone, N. America); *green* continental arc (N. America: Mt. Saint Helens, Three Sisters, McCoy Mountain Complex). **a** Hf versus U/Yb. **b** Sm versus Gd/Yb

to continental arc-type silicic environments. Instead, they most closely resemble silicic magmas from modern, evolving continental rift and continental hotspot environments (e.g. higher Gd/Yb and U/Yb ratios, lower Hf abundances; see Fig. 9; e.g. Carley et al. 2014; Claiborne et al. 2010b). Only a few zircons, mostly from granodiorite (IA-NS-7), fall outside of these fields.

The zircon population from the coastal gabbro (IA-G-1) generally forms the most coherent individual geochemical array. This zircon population likely reflects crystallization within internally fractionating parental melts that experienced little to no interactions with other magmas after the onset of zircon saturation and crystallization. The zircon population from the granophyre (IA-NS-2), in contrast, is the most variable in composition, which may reflect sampling of different growth regions in the complexly zoned zircon grains during analyses. The geochemical variability between zircon growth zones (made visible by CL imaging; see Fig. 4) is likely a consequence of partial mixing and assimilation between multiple batches of silicic magma with differing composition prior to zircon saturation, which resulted in a geochemically heterogeneous magma from which zircons then crystallized. In contrast, the granodiorite (IA-NS-7) and, to a lesser extent, the diorite (IA-NS-6) have elementally bimodal zircon populations best identified by Eu/Eu* and Nb/Yb (IA-NS-7; Fig. 5), and Th, Sc, and Y abundances (IA-NS-6; Fig. 5, Table 2). A substantial number of grains from the diorite, and some in the granodiorite, are anhedral, often with truncated CL zoning surrounded by growth zoning in overgrowth regions in the zircon crystals (Fig. 4), indicating resorption as a consequence of disequilibrium (i.e. undersaturation) between zircons and melt. A rough majority of zircons with resorption and overgrowth zoning in the granodiorite (IA-NS-7) can be correlated with the high-Eu/Eu*, low-Nb population (see Fig. 5). These crystals were analyzed for their interior/core chemistry (see supplementary figure S2). Similarly, analyzed zircons with resorption and overgrowth zoning in the diorite (IA-NS-6) largely fall into the low-Th, low-Sc, low-Y population. These disequilibrium zoning features, and their associated geochemistry, support the open-system interactions suggested by complex mafic–silicic interactions at sampling locations in the field (Table 1; see also "Field interpretations" section above). Thus, we interpret these intermediate units to represent hybridized magmas, resulting from repeated stages of mafic magma replenishment into the silicic pluton and mixing of multiple magma batches with contrasting compositions. The elementally bimodal zircon populations observed in these samples likely represent (1) zircons that crystallized from the silicic end-member prior to mixing with more mafic melt (grains that preserve resorption and overgrowth zoning features), and (2) zircons that crystallized from the resulting hybridized melt, after mixing with the intruding mafic melt.

Our estimated zircon crystallization temperatures for silicic samples, based on Ti compositions (5–40 ppm; Fig. 5d; see Table S3), range from 761 to 981 °C. Maximum Ti-in-zircon temperatures approximately equal zircon saturation temperatures (ZSTs) in the most silicic sample for which zircons were analyzed (granophyre IA-NS-2; 846 °C; Fig. 10). The majority of zircon crystallization temperatures for the granodiorite (IA-NS-7) also fall near

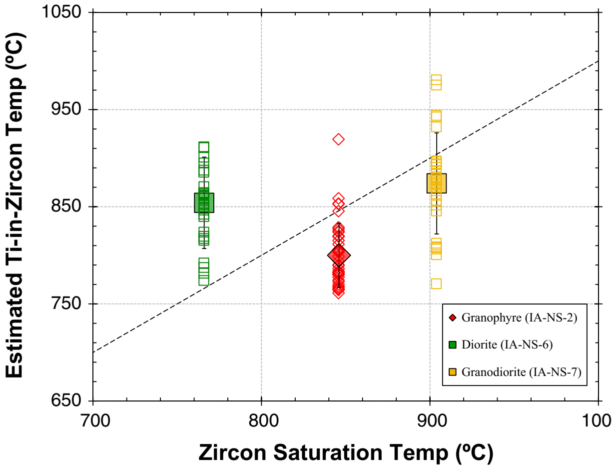

Fig. 10 Estimated whole-rock zircon saturation temperatures (ZST), calculated using the formula derived by Watson and Harrison (1983) as revised by Boehnke et al. (2013), plotted against model zircon crystallization temperatures, calculated using the Ti-in-zircon thermometer of Ferry and Watson (2007), for silicic units of the AIC. The *large filled symbols* represent the mean Ti-in-zircon crystallization temperature for each sample. *Error bars* are 1σ. The *dashed line* indicates a ratio of 1. The diorite sample likely represents a hybrid whose ZST is meaningless

or below the ZST for their host rock (~904 °C). Minimum Ti-in-zircon temperatures are similar for all silicic samples (~760 to 770 °C). The diorite sample (IA-NS-6) has a lower ZST than the silicic samples (766 °C), but its range of Ti-in-zircon temperatures is very similar (774 to 912 °C), especially to the granodiorite. These data together suggest that zircon saturation occurred at roughly 900 °C and zircon crystallization continued to the solidus below 760 °C. The presence of zircons with crystallization temperatures of ~900 °C in a diorite with a ZST of 766 °C reinforces our interpretation that the diorite sample represents a hybridized magma; its ZST is therefore not meaningful because the elemental composition of that sample is far from the original melt composition(s). Ti-in-zircon crystallization temperatures in MSCZ gabbros range from 752 to 981 °C. This likely represents the approximate temperature range from zircon saturation to the solidus for these internally fractionating mafic magmas.

Zircon populations in all but one of our samples (coastal gabbro IA-G-1) preserve a range in δ^{18}O that is greater than analytical uncertainty, which reflects the open-system processes that constructed the MSCZ. The δ^{18}O of MSCZ zircon crystals is both low and variable (+2.2 to +4.8 ‰; Fig. 7; see also Table S5). The expected values for zircon equilibrated with mantle-derived magmas are generally accepted to be in the range of +5.3 ± 0.6 ‰ (e.g. Valley et al. 1998; Bindeman et al. 2008; Drew et al. 2013). Studies of oxygen isotopes in Icelandic magmatic systems (e.g. Maclennan et al. 2003; Thirlwall et al. 2006) suggest that the δ^{18}O signature of the Iceland mantle plume may be substantially lighter than that of typical mantle, based on δ^{18}O values as low as +3.2 to +4.0 ‰ in primary olivines from uncontaminated mantle-derived basaltic magmas. A magma crystallizing olivine with δ^{18}O of +3.2 would permit crystallization of zircons with values as low as ~3.5 ‰ (based on ^{18}O magmatic fractionation differences between zircon and olivine: $\Delta^{18}O_{Zrc-Ol} \approx +0.3$ ‰; Valley et al. 1998; Bindeman 2008). However, the zircon population from the coastal gabbro (IA-G-1), which is the least variable in oxygen isotopic composition (individual zircon values range from +4.2 to +4.9 ‰; see Fig. 7), suggests that the mantle-derived parental mafic melts of the AIC have a nearly homogeneous δ^{18}O > +4.2 ‰. The geochemical composition of the coastal gabbro is the most consistent with closed-system fractionation, and there are no significant interactions observed in the field between the coastal gabbro and silicic magmas in the MSCZ. This supports our interpretation above. In addition, Bindeman et al. (2012) present zircon δ^{18}O values for an intermediate sample (~65 wt% SiO_2) from Austurhorn that range from +4.4 to +5.6 ‰, which they interpret as evidence of fractional crystallization of mantle-derived mafic magmas. These δ^{18}O values are consistent with our interpretation (above) for the signature of the mantle source for the AIC.

Taking into consideration the fraction of zircons with lower than normal δ^{18}O in AIC silicic units (~85 % if we assume normal source magmas are >+4.2 ‰, per our coastal gabbro above), this would indicate that incorporation of hydrothermally altered low-δ^{18}O crust played a major role in the petrogenesis of MSCZ silicic melts with lower and more variable δ^{18}O (down to +2.2 ‰; see Fig. 7; e.g. Martin and Sigmarsson 2010). Intruding mafic magmas likely encountered strongly hydrothermally altered country rock during or after intrusion, or as a consequence of mingling with altered materials in the MSCZ, resulting in melting and variable assimilation of low-δ^{18}O crust, and subsequently facilitating the generation, accumulation, and emplacement of silicic melts in the MSCZ (e.g. Sigmarsson et al. 1991; Bindeman et al. 2008, 2012; Gurenko et al. 2015). Assuming a primary mantle-derived magma signature of +4.2 ‰, generating the low-δ^{18}O observed in zircon crystals from the silicic units would require substantial but variable contribution from preexisting crust that was hydrothermally altered in the presence of meteoric (isotopically light) fluids. If we assume a zircon-equivalent δ^{18}O value of 0 ‰ for altered Icelandic crust (e.g. Gautason and Muehlenbachs 1998; Pope et al. 2013) and +4.2 ‰ for mantle-derived magma, it would require a nearly ~50 % crustal mass fraction in a hybrid magma to crystallize zircons with δ^{18}O of +2.2 ‰ (the lowest MSCZ value). If the altered crust were as low as −5 ‰, the required crustal fraction would be ~20 %.

The elemental data for zircons from the granophyre suggest that contamination by altered crust occurred prior to zircon saturation in the initial magma(s) and was followed by fractionation and zircon crystallization from a compositionally variable melt. In contrast, the multiple populations of zircons in the diorite (IA-NS-6) and granodiorite (IA-NS-7) indicate that some zircon growth had taken place in a range of different melt compositions prior to contamination and mechanical mixing of their host magmas and continued down to the solidus. The wide range of $\delta^{18}O$ in zircons from the sheet gabbro (IA-G-5) suggests that they are in part derived from the host silicic magma through mechanical interactions during intrusion.

Hafnium isotope ratios in zircons further constrain identification of the mantle and/or crustal contributions to the AIC (e.g. Kemp et al. 2007). If the observed O heterogeneity in AIC zircons discussed above was driven by isotopic diversity of the mantle source, we might expect to see a correlative Hf isotope heterogeneity in the same zircon populations. However, the Hf isotopic compositions of MSCZ zircons record minor variability, clustering around a mean of +13 ε-units (±1.6, 2σ SD; see Fig. 7b; see Table S6). These values fall within the lower, less-depleted portion of the whole-rock Hf isotopic range of Icelandic basalts, including the off-rift and lowest end of the on-rift range (Peate et al. 2010; Fig. 7b). The observed range in whole-rock Hf compositions for our samples also overlaps with that of zircons from all MSCZ units (Fig. 11). This suggests that MSCZ magmas were sourced from an off-rift or propagating rift environment. This interpretation is consistent with previous suggestions of a transitional rift location, away from the main rift axis and significantly influenced by the Iceland plume. Furthermore, the relative Hf isotope homogeneity of AIC zircons combined with the heterogeneous $\delta^{18}O$ signature measured in the same zircon populations, as well as the nearly homogeneous $\delta^{18}O$ and ε_{Hf} isotopic composition of coastal gabbro zircons (sample IA-G-1, our best candidate for uncontaminated mantle geochemistry in the AIC), suggests little compositional variability in the Iceland plume in southeast Iceland at the time of magmatic intrusion of the AIC (cf. Martin et al. 2011).

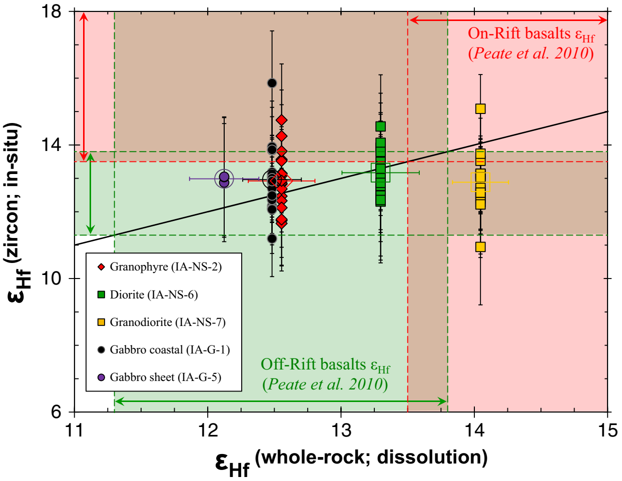

Fig. 11 In situ zircon versus whole-rock ε_{Hf} compositions for units of the AIC. The *larger open symbols* for each sample represent the mean in situ ε_{Hf}, plotted against WR values and their *errors* (2σ). The *red* and *green* zones and *arrows* indicate the ε_{Hf} range of Icelandic *on-rift* basalts (from the Northern and Western Volcanic Zones: $\varepsilon_{Hf} = +13.5$ to $+18.9$; Peate et al. 2010) and *off-rift* basalts (from the Eastern Volcanic Zone, Snæfellsnes Peninsula, Vestmannæyjar, and Snæfell volcano: $\varepsilon_{Hf} = +11.3$ to $+13.8$; Peate et al. 2010), respectively. The *solid black line* indicates a ratio of 1

The in situ U–Pb zircon geochronology data (Fig. 8) permit two different interpretations regarding the construction and longevity of the AIC. When all samples are pooled together, they yield a mean age of 6.52 ± 0.03 Ma for the MSCZ (Fig. 8). This zircon-based age is consistent with the previously published K–Ar age of 6.6 ± 0.4 (2σ SE) Ma (Moorbath et al. 1968) for gabbro, as well as LA-ICP-MS U–Pb zircon ages of 6.6 ± 0.4 and 6.5 ± 0.2 (2σ SE) Ma for granophyre and gabbro, respectively (Martin et al. 2011). The pooled age data may permit a single coherent population that represents one age for the entire complex. However, the MSWD for the number of individual zircon analyses (MSWD = 1.8; $n = 137$) exceeds the upper limit of the 95 % confidence interval (Mahon 1996), suggesting scatter beyond what would be expected for a single statistically coherent population. Alternatively, weighted mean ages for individual samples are statistically distinguishable at 2σ uncertainties and suggest zircons crystallized in the AIC for 320 ± 100 kyr as a result of repeated magmatic intrusions (from approximately 6.67 to 6.35 Ma; Fig. 8). This may be interpreted to represent the approximate timescale of construction of the AIC. We favor this interpretation, which is consistent with the composite field relationships that are preserved in the MSCZ.

Our oldest ages are derived from the homogeneous granophyre bodies near the structural top of the MSCZ and the larger bodies of gabbros within the MSCZ. The field relationships that these units preserve suggest that they experienced limited interaction with other magmas during or after their intrusion. Thus, they likely record the earliest batches of magma that intruded the upper crust at Austurhorn, perhaps initiating the construction of the MSCZ. Subsequent intrusions of magma, especially those with more silicic compositions, experienced more extensive interactions, mixing, and even hybridization. These units indicate that the AIC system was periodically rejuvenated by repeated intrusions of younger, hotter mafic magmas, providing additional heat into the system. This magmatic replenishment prolonged the window of zircon crystallization in silicic magmas as well as the longevity of the Austurhorn magmatic system.

Conclusions

With this study, we present the first detailed characterization of Iceland's plutonic (and likely dominant) zircon population. Both mafic and silicic rocks from the AIC contain a significantly greater abundance of zircons than is typical of Iceland's silicic volcanic rocks. These plutonic zircons are generally larger and display more distinct and complex zoning than volcanic zircons. Grain morphology is varied, and growth-zoned euhedral grains are common in all samples. However, a large number of zircon grains retain evidence, as irregular cores and truncated internal zoning, for thermal and chemical fluctuations that mark repeated mafic–silicic magma interactions in the history of the complex.

The elemental composition of AIC zircons forms a broad but coherent array that mostly overlaps with the well-constrained signature of zircons from Icelandic silicic volcanic rocks. Titanium concentrations range from 5 to 40 ppm (Ti-in-zircon temperatures ~750–990 °C, assuming $a_{\mathrm{TiO2}} = 0.5$ and $a_{\mathrm{SiO2}} = 1.0$), and Hf concentrations are relatively low (below 12,000 ppm), as is typical of Icelandic zircons. Oxygen isotope (δ^{18}O) values extend from +2.2 to +4.8 ‰, consistent with the δ^{18}O range of other Icelandic magmatic zircons from silicic volcanic centers and provide strong evidence for the influence of meteoric water, hydrothermal processes, and recycling of hydrothermally altered crust as a major contribution to silicic magmas within the AIC system. Both whole-rock and zircon epsilon-Hf values cluster around +13, toward the lower end of previously measured values for Iceland basalts. They are similar to those from off-rift settings and the least depleted (lowest $\varepsilon_{\mathrm{Hf}}$) on-rift basalts. This suggests that Austurhorn likely developed in a transitional rift environment, strongly influenced by the Iceland plume.

In situ U–Pb zircon dating yields a weighted mean age of 6.52 ± 0.03 Ma for the entire complex. The spread in average ages for each unit suggests that the construction and evolution of the AIC took place over ~320 kyr. Multiple short-lived intrusion events occurring closely spaced in time from ~6.67 to ~6.35 Ma allowed for periodic rejuvenation and a prolonged lifetime for the crystallizing mush.

Field relationships, whole-rock geochemistry, and the zircon geochemical record of the AIC reveal extensive interaction between mafic and silicic magmas, as part of a very complex silicic magmatic system characterized by multiple episodes of mafic magmatic replenishment. The AIC provides a useful example of the manifestation and consequences of mafic recharge in silicic systems at shallow depths. It adds a valuable dimension in helping us better understand the accumulation of silicic magmas and the subsequent evolution of silicic magmatic systems within the Earth's crust.

Acknowledgments We are grateful to Tanya Furman for her guidance in the planning stages of the Austurhorn project. We thank Aaron Covey (Vanderbilt University), Diane Wilford (Washington State University), Charles Knaack (Washington State University), Brad Ito (Stanford-USGS SHRIMP-RG Lab), and Rebecca Lam (Memorial University of Newfoundland) for their assistance in analytical work. We also thank Guilherme Gualda for his insightful comments and generous review of an earlier version of this manuscript and two anonymous reviewers for their valuable feedback as well as editor Dr. Timothy Grove for guidance during the review process. This work was made possible by the financial support of the National Science Foundation (Research Grant EAR-1220523), the Geological Society of America (Graduate Student Research Grant #9264-10), and the Vanderbilt University Department of Earth Sciences. The ion microprobe facility at UCLA is partly supported by a grant from the Instrumentation and Facilities Program, Division of Earth Sciences, National Science Foundation.

References

Barth AP, Wooden JL (2010) Coupled elemental and isotopic analyses of polygenetic zircons from granitic rocks by ion microprobe, with implications for melt evolution and the sources of granitic magmas. Chem Geol 277(1–2):149–159

Bindeman I (2008) Oxygen isotopes in mantle and crustal magmas as revealed by single crystal analysis. In: Putirka KD, Tepley FJ (eds) Minerals, inclusions and volcanic processes. Reviews in mineralogy and geochemistry, vol 69. Mineralogical Society of America, Washington, DC, pp 602–622

Bindeman I, Gurenko A, Sigmarsson O, Chaussidon M (2008) Oxygen isotope heterogeneity and disequilibria of olivine crystals in large volume Holocene basalts from Iceland: evidence for magmatic digestion and erosion of Pleistocene hyaloclastites. Geochim Cosmochim Acta 72:4397–4420

Bindeman I, Gurenko A, Carley TL, Miller CF, Martin E, Sigmarsson O (2012) Silicic magma petrogenesis in Iceland by remelting of hydrothermally altered crust based on oxygen isotope diversity and disequilibria between zircon and magma with implications for MORB. Terra Nova 24(3):227–232

Black LP, Kamo SL, Allen CM, Davis DW, Aleinikoff JN, Valley JW, Mundil R, Campbell IH, Korsuch RJ, Williams IS, Foudoulis C (2004) Improved 206Pb/238U microprobe geochronology by the monitoring of a trace-element-related matrix effect; SHRIMP, ID–TIMS, ELA–ICP–MS and oxygen isotope documentation for a series of zircon standards. Chem Geol 205:115–140

Blake DH (1966) Net-veined complex of Austurhorn Intrusion, Southeastern Iceland. Geology 74(6):891–907

Blake DH (1970) Geology of Alftafjordur volcano, a Tertiary volcanic centre in South-Eastern Iceland. Sci Isl 2:43–63

Boehnke P, Watson EB, Trail D, Harrison TM, Schmitt AK (2013) Zircon saturation re-visited. Chem Geol 351:324–334

Bouvier A, Vervoort JD, Patchett PJ (2008) The Lu–Hf and Sm–Nd isotopic composition of CHUR: constraints from unequilibrated chondrites and implications for the bulk composition of terrestrial planets. Earth Planet Sci Lett 273:48–57

Carley TL, Miller CF, Wooden JL, Bindeman IN, Barth AP (2011) Zircon from historic eruptions in Iceland: reconstructing storage and evolution of silicic magmas. Mineral Petrol 102:135–161

Carley TL, Miller CF, Wooden JL, Padilla AJ, Schmitt AK, Economos RC, Bindeman IN, Jordan BT (2014) Iceland is not a magmatic analog for the Hadean: evidence from the zircon record. Earth Planet Sci Lett 405:85–97

Cherniak DJ, Watson EB (2000) Pb diffusion in zircon. Chem Geol 172:5–24

Cherniak DJ, Watson EB (2007) Ti diffusion in zircon. Chem Geol 242:470–483

Cherniak DJ, Hanchar JM, Watson EB (1997a) Diffusion of tetravalent cations in zircon. Contrib Miner Petrol 127:383–390

Cherniak DJ, Hanchar JM, Watson EB (1997b) Rare-earth diffusion in zircon. Chem Geol 134:289–301

Claiborne LL, Miller CF, Walker BA, Wooden JL, Mazdab FK, Bea F (2006) Tracking magmatic processes through Zr/Hf ratios in rocks and Hf and Ti zoning in zircons: an example from the Spirit Mountain batholith, Nevada. Mineral Mag 70(5):517–543

Claiborne LL, Miller CF, Flanagan DM, Clynne MA, Wooden JL (2010a) Zircon reveals protracted magma storage and recycling beneath Mount St. Helens. Geology 38(11):1011–1014

Claiborne LL, Miller CF, Wooden JL (2010b) Trace element composition of igneous zircon: a thermal and compositional record of the accumulation and evolution of a large silicic batholith, Spirit Mountain, Nevada. Contrib Miner Petrol 160:511–531

Corfu F, Hanchar JM, Hoskin PWO, Kinny P (2003) Atlas of zircon textures. In: Hanchar JM, Hoskin PWO (eds) Zircon. Reviews in mineralogy and geochemistry, vol 53. Mineralogical Society of America, Washington, DC, pp 27–62

Drew DL, Bindeman IN, Watts KE, Schmitt AK, Fu B, McCurry M (2013) Crustal-scale recycling in caldera complexes and rift zones along the Yellowstone hotspot track: O and Hf isotopic evidence in diverse zircons from voluminous rhyolites of the Picabo volcanic field, Idaho. Earth Planet Sci Lett 381:63–77

Ferry JM, Watson EB (2007) New thermodynamic models and revised calibrations for the Ti-in-zircon and Zr-in-rutile thermometers. Contrib Miner Petrol 154:429–437

Fisher CM, Hanchar JM, Samson SD, Dhuime B, Blichert-Toft J, Vervoort JD, Lam R (2011) Synthetic zircon doped with hafnium and rare earth elements: a reference material for in situ hafnium isotope analysis. Chem Geol 286(1):32–47

Fisher CM, Vervoort JD, Hanchar JM (2014) Guidelines for reporting zircon Hf isotopic data by LA–MC–ICPMS and potential pitfalls in the interpretation of these data. Chem Geol 363:125–133

Furman TH (1989) Evolution of Icelandic central volcanoes: evidence from the Austurhorn Plutonic and Vestmannaeyjar volcanic complexes. Ph.D. Dissertation, Massachusetts Institute of Technology/Woods Hole Oceanographic Institution Joint Program, 373 pp

Furman T, Meyer PS, Frey FA (1992a) Evolution of Icelandic central volcanoes: evidence from the Austurhorn intrusion, southeastern Iceland. Bull Volc 55:45–62

Furman T, Frey FA, Meyer PS (1992b) Petrogenesis of evolved basalts and rhyolites at Austurhorn, southeastern Iceland: the role of fractional crystallization. J Petrol 33:1405–1445

Gale NH, Moorbath S, Simons J, Walker GPL (1966) K–Ar ages of acid intrusive rocks from Iceland. Earth Planet Sci Lett 1:284–288

Gautason B, Muehlenbachs K (1998) Oxygen isotopic fluxes associated with high-temperature processes in the rift zones of Iceland. Chem Geol 145:275–286

Ghiorso MS, Gualda GAR (2013) A method for estimating the activity of titania in magmatic liquids from the compositions of coexisting rhombohedral and cubic iron–titanium oxides. Contrib Miner Petrol 165:73–81

Grimes CB, John BE, Kelemen PB, Mazdab FK, Wooden JL, Cheadle MJ, Hanghøj K, Schwartz JJ (2007) Trace element chemistry of zircons from oceanic crust: a method for distinguishing detrital zircon provenance. Geology 35(7):643–646

Grimes CB, Wooden JL, Cheadle MJ, John BE (2015) “Fingerprinting” tectono-magmatic provenance using trace elements in igneous zircon. Contrib Miner Petrol 170:46

Gunnarsson B, Marsh BD, Taylor HP (1998) Generation of Icelandic rhyolites: silicic lavas from the Torfajokull central volcano. J Volcanol Geoth Res 83:1–45

Gurenko AA, Bindeman IN, Sigurdsson IA (2015) To the origin of Icelandic rhyolites: insights from partially melted leucocratic xenoliths. Contrib Miner Petrol 169:49

Harper BE, Miller CF, Koteas GC, Cates NL, Wiebe RA, Lazzareschi DS, Cribb JW (2004) Granites, dynamic magma chamber processes and pluton construction: the Aztec Wash pluton, Eldorado Mountains, Nevada, USA. Trans R Soc Edinb Earth Sci 95:277–295

Harrison TM, Watson EB, Aikman AB (2007) Temperature spectra of zircon crystallization in plutonic rocks. Geology 35(7):635–638

Hoskin PWO, Schaltegger U (2003) The composition of zircon and igneous and metamorphic petrogenesis. In: Hanchar JM, Hoskin PWO (eds) Zircon. Reviews in Mineralogy and Geochemistry, vol 53. Mineralogical Society of America, Washington DC, pp 27–62

Jónasson K (2007) Silicic volcanism in Iceland: composition and distribution within the active volcanic zones. J Geodyn 43:101–117

Kemp AIS, Hawkesworth CJ, Foster GL, Paterson BA, Woodhead JD, Hergt JM, Gray CM, Whitehouse MJ (2007) Magmatic and crustal differentiation history of granitic rocks from Hf–O isotopes in zircon. Science 315(5814):980–983

Ludwig KR (2009) Unpublished–SQUID 2 data reduction program. Berkeley Geochronology Center. http://www.bgc.org/isoplot_etc/squid.html

Maclennan J, McKenzie D, Grönvold K, Shimizu N, Eiler JM, Kitchen N (2003) Melt mixing and crystallization under Theistareykir, northeast Iceland. Geochem Geophys Geosyst 4(11):8624

Mahon KI (1996) The New “York” regression: application of an improved statistical method to geochemistry. Int Geol Rev 38:293–303

Martin E, Sigmarsson O (2007) Crustal thermal state and origin of silicic magma in Iceland: the case of Torfajökull, Ljósufjöll and Snæfellsjökull volcanoes. Contrib Miner Petrol 153:593–605

Martin E, Sigmarsson O (2010) Thirteen million years of silicic magma production in Iceland: links between petrogenesis and tectonic settings. Lithos 116:129–144

Martin E, Paquette JL, Bosse V, Ruffet G, Tiepolo M, Sigmarsson O (2011) Geodynamics of rift-plume interaction in Iceland as constrained by new ^{40}Ar/^{39}Ar and in situ U–Pb zircon ages. Earth Planet Sci Lett 311:28–38

Mattson SR, Vogel TA, Wilband JT (1986) Petrochemistry of the silicic–mafic complexes at Vesturhorn and Austurhorn, Iceland: evidence for zoned/stratified magma. J Volcanol Geoth Res 28:197–223

McDowell SM, Miller CF, Mundil R, Ferguson CA, Wooden JL (2014) Zircon evidence for a ~200 k.y. supereruption-related thermal flare-up in the Miocene southern Black Mountains, western Arizona, USA. Contrib Miner Petrol 168:1031

Miller CF, McDowell SM, Mapes RW (2003) Hot and cold granites? Implications of zircon saturation temperatures and preservation of inheritance. Geology 31:529–532

Moecher DP, McDowell SM, Samson SD, Miller CF (2014) Ti-in-zircon thermometry and crystallization modeling support hot Grenville granite hypothesis. Geology 42:267–270

Moorbath S, Sigurdsson H, Goodwin R (1968) K–Ar ages of the oldest exposed rocks in Iceland. Earth Planet Sci Lett 4:197–205

Padilla AJ (2015) Elemental and isotopic geochemistry of crystal-melt systems: elucidating the construction and evolution of silicic magmas in the shallow crust, using examples from southeast Iceland and southwest USA. Ph.D. Dissertation, Vanderbilt University

Pamukcu AS, Carley TL, Gualda GAR, Miller CF, Ferguson CA (2013) The evolution of the Peach Spring giant magma body: evidence from accessory mineral textures and compositions, bulk pumice and glass geochemistry, and rhyolite-MELTS modeling. J Petrol 54:1109–1148

Peate DW, Breddam K, Barker JA, Kurz MD, Barker AK, Prestvik T, Grassineau N, Skovgaard AC (2010) Compositional characteristics and spatial distribution of enriched Icelandic mantle components. J Petrol 51(7):1447–1475

Pope EC, Bird DK, Arnorsson S (2013) Evolution of low-O-18 Icelandic crust. Earth Planet Sci Lett 374:47–59

Ross JG, Mussett AE (1976) ^{40}Ar/^{39}Ar dates for spreading rates in eastern Iceland. Nature 259(5538):36–38

Sigmarsson O, Hémond C, Condomines M, Fourcade S, Oskarsson N (1991) Origin of silicic magma in Iceland revealed by Th isotopes. Geology 19:621–624

Thirlwall MF, Gee MAM, Lowry D, Mattey DP, Murton BJ, Taylor RN (2006) Low d18O in the Icelandic mantle and its origins: evidence from Reykjanes Ridge and Icelandic lavas. Geochim Cosmochim Acta 70:993–1019

Thorarinsson SB, Tegner C (2009) Magma chamber processes in central volcanic systems of Iceland: constraints from layered gabbro of the Austurhorn intrusive complex. Contrib Miner Petrol 158:223–244

Thordarson T, Höskuldsson A (2002) Iceland–classic geology in Europe 3. Terra Publishing, Edinburgh

Trail D, Mojzsis SJ, Harrison TM, Schmitt AK, Watson EB, Young ED (2007) Constraints on Hadean zircon protoliths from oxygen isotopes, Ti-thermometry, and rare earth elements. Geochem Geophys Geosyst 8:22

Valley JW (2003) Oxygen isotopes in zircon. In: Hanchar JM, Hoskin PWO (eds) Zircon. Reviews in mineralogy and geochemistry, vol 53. Mineralogical Society of America, Washington, DC, pp 344–385

Valley JW, Kinny PD, Schulze DJ, Spicuzza MJ (1998) Zircon megacrysts from kimberlite: oxygen isotope variability among mantle melts. Contrib Miner Petrol 133:1–11

Veblem DR, Buseck PR (1981) Hydrous pyriboles and sheet silicates in pyroxenes and uralites: intergrowth microstructures and reaction mechanisms. Am Mineral 66:1107–1134

Vernon RH (1984) Microgranitoid enclaves in granites—globules of hybrid magma quenched in a plutonic environment. Nature 309(5967):438–439

Vervoort JD, Blichert-Toft J (1999) Evolution of the depleted mantle: Hf isotope evidence from juvenile rocks through time. Geochim Cosmochim Acta 63:533–556

Walker GPL (1960) Zeolite zones and dike distribution in relation to the structure of the basalts of eastern Iceland. J Geol 68:515–527

Walker GPL (1964) Geological investigations in eastern Iceland. Bull Volc 27:1–15

Walker GPL (1966) Acid volcanic rocks in Iceland. Bull Volc 29:375–402

Watson EB, Cherniak DJ (1997) Oxygen diffusion in zircon. Earth Planet Sci Lett 148(3–4):527–544

Watson EB, Harrison TM (1983) Zircon saturation revisited: temperature and composition effects in a variety of crustal magma types. Earth Planet Sci Lett 64:295–304

Weidendorfer D, Mattsson HB, Ulmer P (2014) Dynamics of magma mixing in partially crystallized magma chambers: textural and petrological constraints from the basal complex of the Austurhorn Intrusion (SE Iceland). J Petrol 55(9):1865–1903

Wiebe RA, Collins WJ (1998) Depositional features and stratigraphic sections in granitic plutons: implications for the emplacement and crystallization of granitic magma. J Struct Geol 20(9/10):1273–1289

Wiebe RA, Blair KD, Hawkins DP, Sabine CP (2002) Mafic injections, in situ hybridization, and crystal accumulation in the Pyramid Peak granite, California. Geol Soc Am Bull 114:909–920

Wiebe RA, Manon MR, Hawkins DP, McDonough WF (2004) Late-stage mafic injection and thermal rejuvenation of the Vinalhaven Granite, Coastal Maine. J Petrol 45(11):2133–2153

Woodhead JD, Hergt JM (2005) A preliminary appraisal of seven natural zircon reference materials for in situ Hf isotope determination. Geostand Geoanal Res 29(2):183–195